2023

Petrological and Geochemical Evaluation of Rare-Earth Element Potential in the Sparta Granite Complex

Max J. Eshbaugh
Georgia Southern University

Petrological and Geochemical Evaluation of Rare-Earth Element Potential in the Sparta Granite Complex

An Honors Thesis submitted in partial fulfillment of the requirements for Honors in *Geology & Geology*.

By
Max Eshbaugh

Under the mentorship of *Dr. R.K. Vance*

ABSTRACT

Rare earth elements (REEs) are important resources with applications in the electronics, renewable energy, and automotive industries. REEs may be concentrated in the residual weathered portion of igneous parent rocks, typically granites. These residual deposits are mined in southeast Asia, but analogous climatic and geologic conditions suggest the existence of economically viable REE residual deposits in the southeastern United States (U.S.). The Sparta Granite Complex in east-central Georgia is a granitoid complex emplaced at the end of the Alleghanian orogeny, forming a suture between the Savannah River and Milledgeville terranes. Petrologic and geochemical assessments of the Sparta Granite and overlying *in situ* residual deposits elucidate its intrusive history and explore the potential to produce economically significant residual REE deposits. Fresh rock and saprolite were obtained from two aggregate quarries near Sparta, Georgia and one aggregate quarry near Warrenton, Georgia. Field observations of flow brecciation and multiple granitic phases including pegmatitic and aplite dikes indicate significant fractionation. Thin section analysis showed deformation features and strain indicators in feldspars and quartz suggesting a late-kinematic formation. Accessory minerals include zircon, sphene, apatite, and partially to fully metamict allanite. Geochemical data of representative rock samples and saprolite are acquired with inductively coupled plasma mass spectrometry (IC-PMS) and indicated a volcanic arc origin with possible crustal contamination. Major REE sources were garnet and zircon for HREE and allanite, sphene, and apatite for LREE.

Thesis Mentor: *Dr. R.K. Vance*

Honors Dean: Dr. Steven Engel

April 2023
Geology & Geography
Honors College
Georgia Southern University

Table of Contents

ABSTRACT

Rare earth elements (REEs) are important resources with applications in the electronics, renewable energy, and automotive industries. REEs may be concentrated in the residual weathered portion of igneous parent rocks, typically granites. These residual deposits are mined in southeast Asia, but analogous climatic and geologic conditions suggest the existence of economically viable REE residual deposits in the southeastern United States (U.S.). The Sparta Granite Complex in east-central Georgia is a granitoid complex emplaced at the end of the Alleghanian orogeny, forming a suture between the Savannah River and Milledgeville terranes. Petrologic and geochemical assessments of the Sparta Granite and overlying *in situ* residual deposits elucidate its intrusive history and explore the potential to produce economically significant residual REE deposits. Fresh rock and saprolite were obtained from two aggregate quarries near Sparta, Georgia and one aggregate quarry near Warrenton, Georgia. Field observations of flow brecciation and multiple granitic phases including pegmatitic and aplite dikes indicate significant fractionation. Thin section analysis showed deformation features and strain indicators in feldspars and quartz suggesting a late-kinematic formation. Accessory minerals include zircon, sphene, apatite, and partially to fully metamict allanite. Geochemical data of representative rock samples and saprolite are acquired with inductively coupled plasma mass spectrometry (IC-PMS) and indicated a volcanic arc origin with possible crustal contamination. Major REE sources were garnet and zircon for HREE and allanite, sphene, and apatite for LREE.

INTRODUCTION

The lanthanide group on the periodic table along with scandium and yttrium are described as the Rare Earth Elements (REEs). REEs can be further divided into two subgroups: light REEs (LREEs), from La to Eu, and heavy REEs (HREEs), from Gd to Lu (da Silva et al, 2017). Despite the name, REEs are fairly ubiquitous in Earth's crust, but they are rarely found in high enough concentrations to be efficiently mined (da Silva et al, 2017; Jin et al, 2017). As of 2022, REEs are classified as "critical minerals" by the U.S. Geological Survey (USGS) due to their numerous technological applications and economic importance (Burton, 2022). Sources of REEs include carbonatites, placer deposits, and pegmatites. Recently, surficial residual deposits consisting of *in situ* weathered material overlying a typically igneous parent rock have garnered attention (Jin et al, 2017).

REE-bearing residual deposits are formed from long periods of intense weathering with little accompanying erosion of an igneous parent rock, typically a granite. The requisite weathering conditions to form a residual deposit are understood to be warm climates with significant rainfall typically found in temperate to subtropical regions. This intense chemical weathering results in a thick regolith layer in which REE mobilization and enrichment has occurred, concentrating REEs in particular layers. A particular subset of residual deposits, ion-adsorption clay deposits, are noteworthy as their high clay content leads to sorption of REEs to clay minerals, especially in the kaolin group (Mukai et al., 2020). Currently, residual deposits are almost exclusively mined in South China, which reports deposits of REE concentrations in the 500-3000 ppm range (Foley et al., 2015). The extraction rate for residual deposits tends to be around 50% for LREEs and potentially up to 70% for HREEs; consequently, residual deposits supply the vast majority of the world's HREE resources (Foley et al., 2015; Mukai et al., 2020). In recent years, the potential for the occurrence of residual deposits in the southeastern United States has been under investigation due to the similar geologic and climatic conditions found in South China (Foley et al., 2015).

While residual deposits are of economic interest due to their REE concentrations, the mechanisms with which REEs mobilize in weathered material is poorly understood, largely due to the variety of influencing factors (da Silva et al., 2017). Despite the general chemical similarities between the various REEs, they do not always behave coherently; particularly between LREEs and HREEs, fractionation of different elements is common in the weathering

environment. In granitic rocks, of which residual deposits typically originate from, REEs mobilize from the dissolution of primary accessory minerals (Yang et al., 2019; Cheshire et al, 2018; Yusoff et al., 2013). Despite the insolubility of REEs, mobilization is still able to occur, and is typically aided by chemical factors such as source rock chemistry, presence and chemistry of fluids, adsorption onto sediments, secondary mineral formation, and complexation (Cheshire et al, 2018; da Silva et al, 2017; Yang et al, 2019; Yusoff et al, 2013). The primary accessory phases that control REE concentration are mostly phosphates (apatite, monazite, xenotime) and certain silicates (allanite, zircon), while secondary carbonate minerals like bastnaesite and parisite also play a role (Cheshire et al, 2018; da Silva et al, 2017; Yusoff et al, 2013).

Geologic Setting

The southeastern flank of the Appalachian mountains consists of a series of Neoproterozoic to early Paleozoic volcanic arc systems referred to as the Carolina Zone. These volcanic arcs are regarded as being exotic to Laurentia in nature, extending from Georgia to Virginia. The Carolina Zone is bounded on the surface by the central Piedmont shear zone in the northwest and the Fall Line in the southeast (Fig. 1), where it is then overlain unconformably by Cretaceous to Tertiary coastal plain sediments. The terranes themselves are composed of metaigneous and metasedimentary rocks. The terranes can be divided into either the "suprastructural" category, in which the rocks have generally remained in the upper crust and as such have experienced only low grade metamorphism, or "infrastructural" category, in which the rocks have been subjected to metamorphism of amphibolite facies or higher in the middle to lower crust (Hibbard et al., 2002).

The Milledgeville terrane is a suprastructural terrane in central Georgia. It consists of northeast-trending greenschist facies phyllite, schist, and quartzite bounded by the Buzzard Island fault to the northwest and Modoc shear zone to the north. Despite significant deformation, primary textures suggest an origin of felsic volcanic rocks, siltstone, and greywacke. Adjacent to the Milledgeville terrane is the infrastructural Savannah River terrane. The Savannah River terrane is an infrastructural terrane composed mostly of biotite-amphibole paragneiss, sillimanite schist, and quartzite. The terrane is bounded on the north by the Modoc shear zone and on the south and east by the Augusta terrane and coastal plane sediments. The nature of the boundary between the Milledgeville and Savannah River terranes is unknown as it is largely covered by

the Sparta granite complex, which is thus considered a stitching pluton between the two terranes (Hibbard et al., 2002).

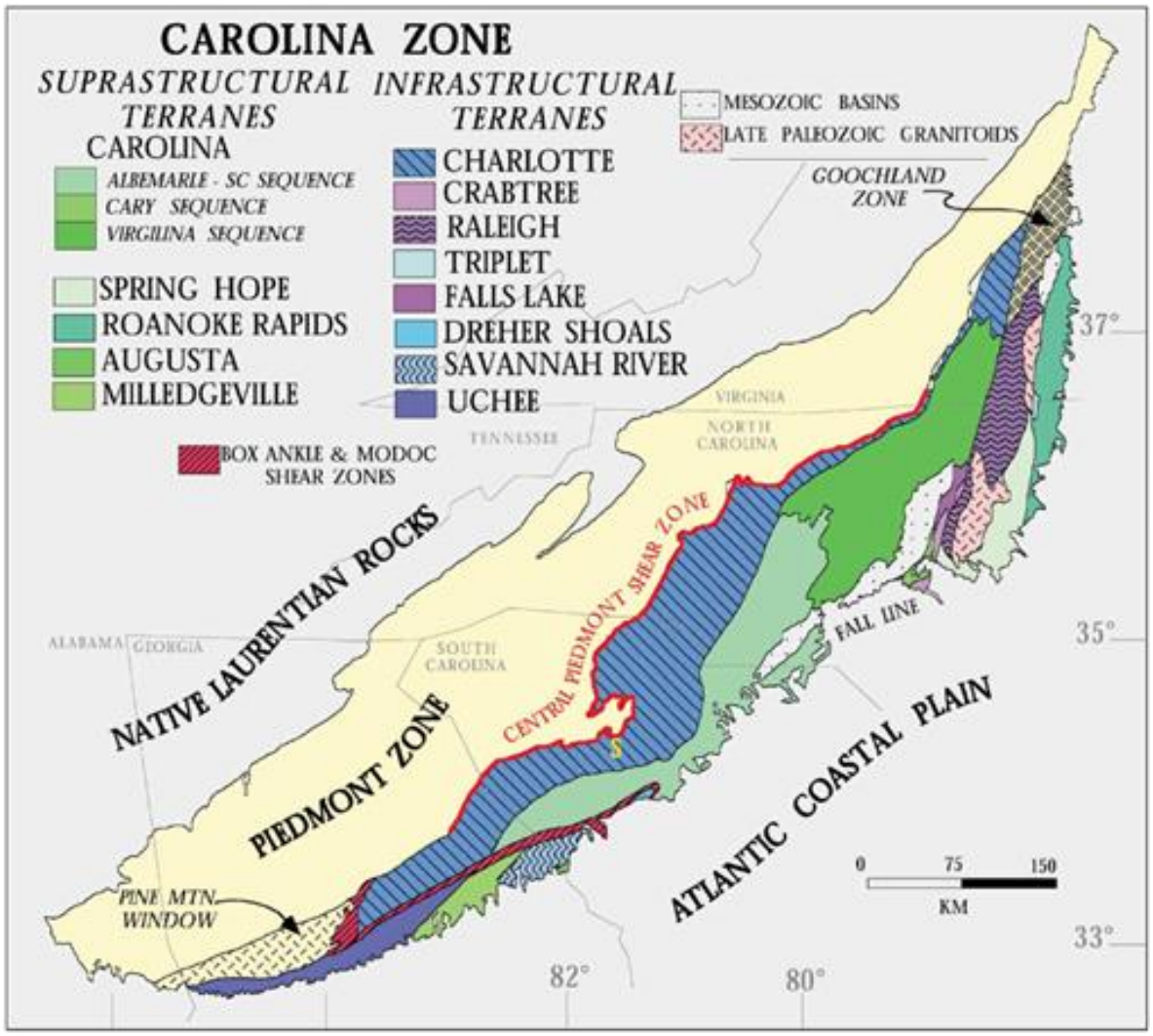

Fig. 1. Overview of the suprastructural and infrastructural terranes that encompass the Carolina Zone (Hibbard et al., 2002)

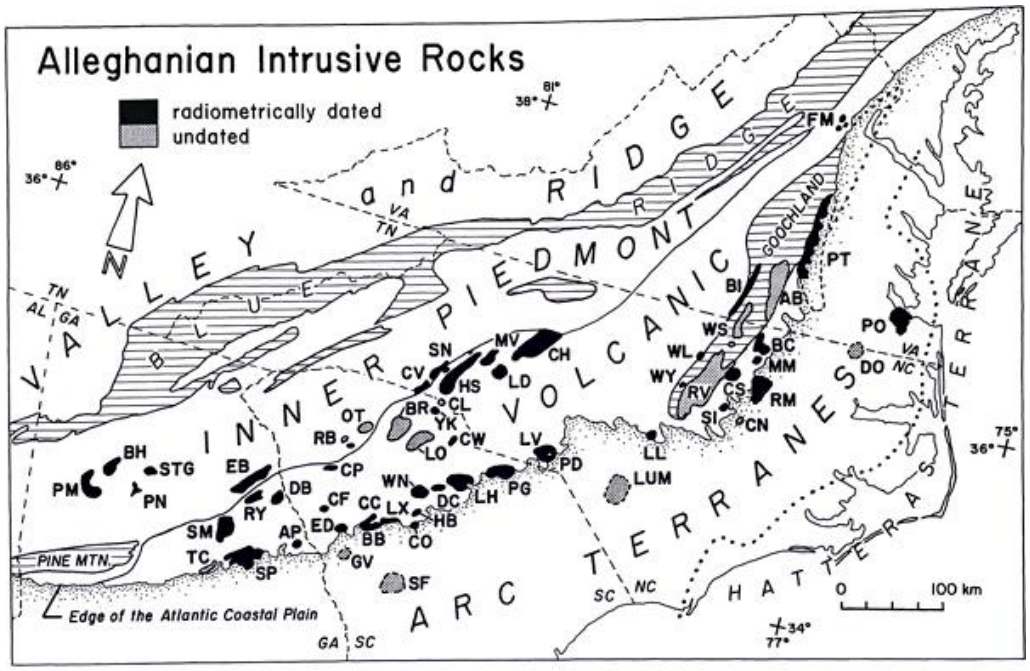

Fig. 2. Locations of Alleghanian plutons in the southern Appalachians. "SP" denotes Sparta Granite (Speer et al., 1994).

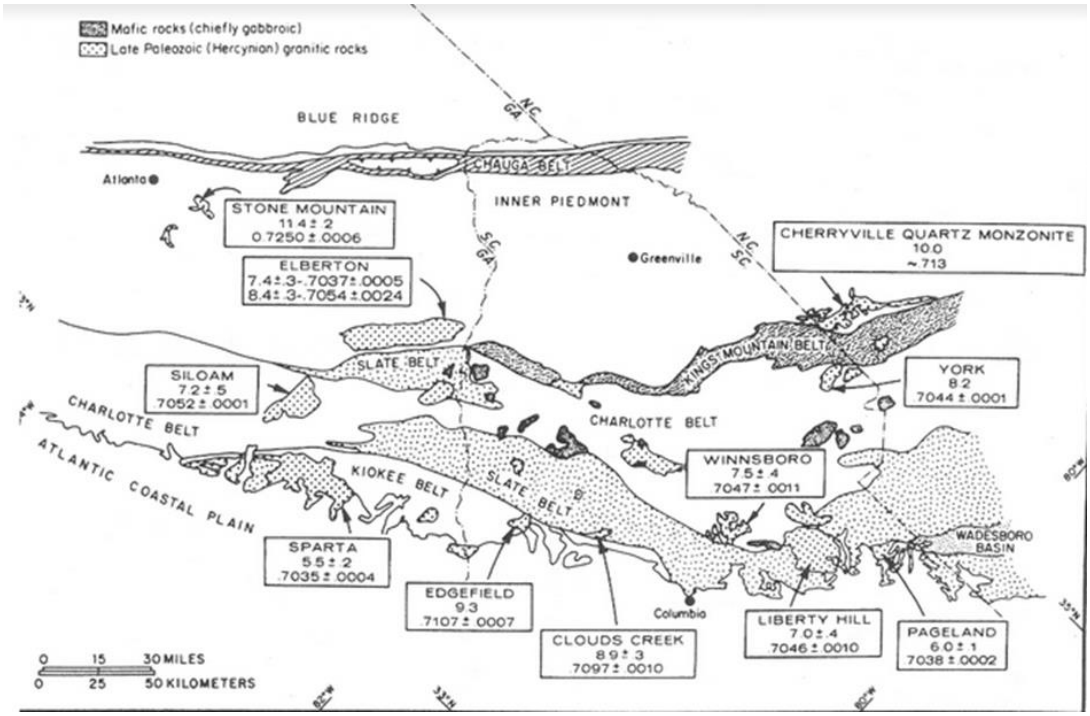

Fig. 3. Detailed map of granitoid plutons in Georgia and South Carolina. Oxygen and strontium isotopic ratios are shown as the top and bottom numbers, respectively (Whitney & Wenner, 1980

SPARTA GRANITE

The Alleghanian orogeny is the third and final major orogenic event in the history of the Appalachian Mountains and is considered to have taken place from around 327 ± 21 Ma to between 286-66 Ma, as defined by the development of the foreland clastic wedge for the Appalachians (Speer at al., 1994). The Alleghanian orogeny resulted in the emplacement of many post-metamorphic plutons in a northeasterly trending distribution across the southern Appalachians (Fig. 1 & 2). A vast majority of these plutons are granitoid in nature, covering around 10,500 km^2, while a few gabbroic plutons cover <60 km^2. The magmatism of the Alleghanian plutons appears to have developed rapidly and with a variety of material sources, and with no temporal or spatial trends in composition. To explain this, several models for magma generation and emplacement are evaluated by Speer et al. (1994), but the most likely appears to be decompression melting from a combination of erosional unloading and crustal arching due to strike-slip fault activity along with the addition of flux assisted by the Alleghanian deformation. Magma segregation and ascent then likely occurred via intrusion into shear zones resulting from the Alleghanian deformation, which then promoted ascent of the magmas to final emplacement depths between 8 and 20 km (Speer et al., 1994).

The Sparta Granite complex is one such Alleghanian pluton. It is considered to be a stitching pluton between the Savannah River and Milledgeville terranes, emplaced in metamorphic country rock consisting of migmatitic gneiss, mica schist, and quartzite (Hibbard et al., 2002; Fullagar and Butler, 1976). Other literature refers to the Sparta Granite complex as part of the Kiokee belt (Whitney and Wenner, 1980). Rb-Sr isotope data gives an age for the complex of 295 ± 2 Ma, which is similar to other plutons in the region and aligns with the latter portion of the Alleghanian orogeny. The Sr^{87}/Sr^{86} isotope ratio is 0.7035 ± 0.0004, which is remarkably low and indicates that there was almost no assimilation of crustal material during magma ascent (Fullagar and Butler, 1976). Multiple textures have been identified, ranging from pegmatitic to aplitic, but all seem to be isotopically related and thus from the same source. The main granitic texture is a medium- to coarse-grained equigranular rock with quartz, oligoclase, microcline, and biotite. Southern portions are described as being texturally similar with the addition of hornblende, but with some chemical differences that may be related to the assimilation of xenoliths and interactions with meteoric water (Whitney and Wenner, 1980; Fullagar and Butler, 1976). Whitney and Wenner (1980) note flow foliation in the granite and a variety of chemical

compositions that suggest differentiation of a parent magma, and even suggest the possibility of multiple magma injections.

The Sparta Granite complex has been recently surveyed by Massey and Vance (2019) and Fischer et al. (2020) in two undergraduate thesis projects. These projects were restricted to an aggregate quarry located near Warrenton, GA and operated by Martin-Marietta Aggregates and focused primarily on the petrology and petrography of the various phases observed in the context of petrogenesis and magmatism of the Alleghanian plutons of the Appalachians. This thesis project will extend the petrologic and petrographic evaluation of the Sparta Granite complex to two additional quarries and place a greater emphasis on geochemical analysis with respect to the potential of the complex to produce REE-bearing residual deposits. This research will provide a basis for understanding how the mineralogy and petrology of the Sparta complex influences the REE content in an area where this particular subject has not been extensively studied.

FIELD WORK

Vulcan Materials Company Quarry

Located near Sparta, GA is an aggregate quarry operated by Vulcan Materials Company. Due to limited pit access, most samples consisted of residual material. Samples were obtained from three sites shown in Fig. 4: a pile of disturbed residual material labelled Site 1 (33.28314°, -82.93496°), rubble from the highest bench labelled Site 2 (33.28886°, -82.93644°), and a 50 foot *in-situ* weathering profile at Site 3 (33.28813°, -82.93510°).

Fig. 4. Overhead view of Vulcan Materials Company Quarry. Sites where samples were collected are marked in yellow (Modified from Google Earth).

Hanson Aggregates Quarry

Located roughly 2.7 miles to the southeast of the Vulcan Material Company Quarry is another quarry operated by Hanson Aggregates. Samples were obtained from three general areas as seen in Fig. 5: rubble from the bottom of the pit, labelled Site 1 (33.25592°, -82.90147°), rubble from the east side of the second lowest bench of the pit, labelled Site 2 (33.25592°, -82.90147°), and recently exposed residual material on the highest level on the northeast side of the pit (33.25732°, -82.90218°).

Fig. 5. Overhead view of Hanson Aggregates Quarry. Sites where samples were collected are marked in yellow (Modified from Google Earth).

Martin Marietta Aggregates Quarry

Located southeast of Warrenton, GA is an aggregate quarry operated by Martin Marietta Aggregates. Samples were obtained from four different locations as seen in Fig. 6: residual material on uppermost bench, labelled Site 1 (33.38127°, -82.64365°), residual material on uppermost bench, labelled Site 2 (33.38097°, -82.64535°), residual material on uppermost bench, labelled Site 3 (33.38089°, -82.64521°), and rubble from the second bench from the top of the pit, labelled Site 4 (33.38040°, -82.64392°).

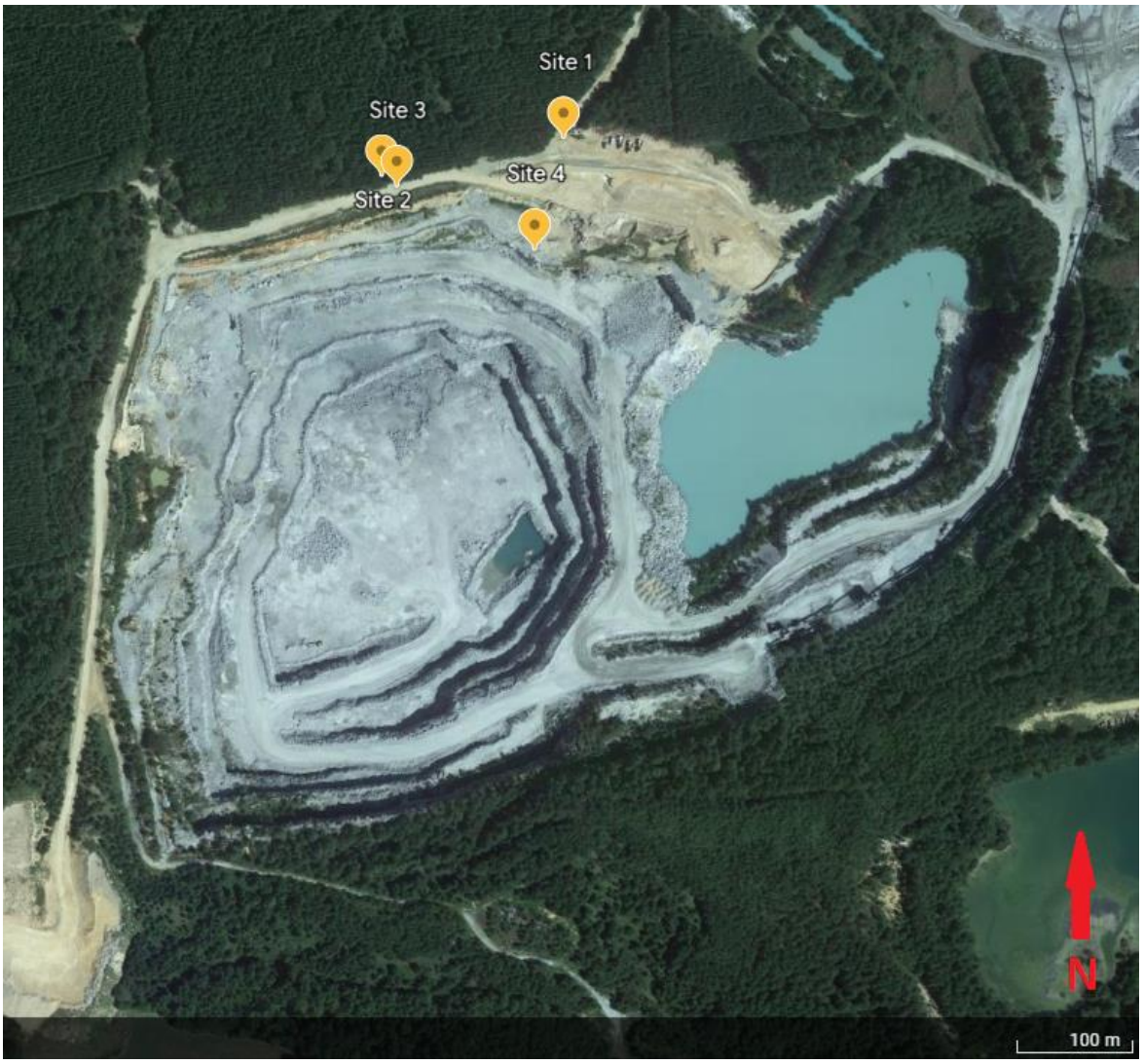

Fig. 6. Overhead view of Martin Marietta Aggregates Quarry. Sites where samples were collected are marked in yellow (Modified from Google Earth).

Field Relations

Due to a lack of access to the main pit portions of the Vulcan and Martin Marietta Quarries, most field observations about the rock phases of the Sparta complex were made at the Hanson Quarry. The main rock phase present in the Hanson Quarry was a medium to coarse grained granite with noticeable biotite foliation (Fig. 7). Flow brecciation was present throughout the Hanson Quarry where large blocks of the main granitic phase were surrounded by a finer grained biotite-rich phase with sharp contacts (Fig. 8). Occasional 5-9 cm wide biotite-rich shear zones were present with visible sigmoidal shear sense indicators (Fig. 9). Numerous pegmatite-aplite dikes were present throughout the quarry with various orientations crosscutting other phases. There is significant variety in the thickness of the dikes, ranging from ~1 cm to several dozen cm. Textural composition was also quite variable, ranging from purely pegmatitic (Fig. 10), purely aplitic (Fig. 11), or to some combination thereof (Fig. 12). Most, if not all, of the quartz present in the aplite-pegmatite phases is of the smoky variety. Sphene and garnet were present in a number of samples, particularly in the pegmatite-aplite phase. Purple fluorite crystals were rarely observed in certain samples. In terms of crosscutting relationships, the biotite shear zones cut through the main phase granite, while the pegmatite-aplite dikes cut through the shear zones (Fig. 13). All phases were crosscut by a large diabase dike spanning the entire quarry profile present at both the Vulcan and Hanson Quarries.

At the Martin Marietta Quarry, three main granitic units were observed: a coarse foliated phase, a finer grained granitic phase, and a coarse pegmatitic granite. Many unevenly spaced joints were observed, possessing surficial iron oxide staining. Migmatite was observed near the gneissic country rock, with minor chlorite and sulfide content. One sample was found with large elongate allanite crystals in alignment (Fig. 14).

The sequence of samples from the weathering profile at the Vulcan Quarry comprised eight samples taken at an interval between four and ten feet up until an unconformity. The weathering profile consisted of roughly 30 feet of saprolite that distinctly retained the original granite texture and 20 feet of B-horizon in which the original texture was largely destroyed. Residual material at the other two quarries was similar, with saprolite zones possessing preserved textures that allowed for identification of weathered pegmatite-aplite dikes. Several of these dikes had measurable strikes: 056°, 066°, 050°, and 335°. The Hanson Quarry did not have a

well-exposed residuum profile, but a kaolin-rich zone above the saprolite zone was commonly present. Saprolite had distinctly retained the original granite texture but with alteration to clay minerals (Fig. 15). Similar observations were made at the Martin Marietta Quarry, along with the presence of large “boulders” of cohesive weathered material and a biotite/vermiculite rich shear zone preserved in the overburden material.

Fig. 7. Main phase of Sparta Granite complex at Hanson Quarry. Note foliation of biotite grains.

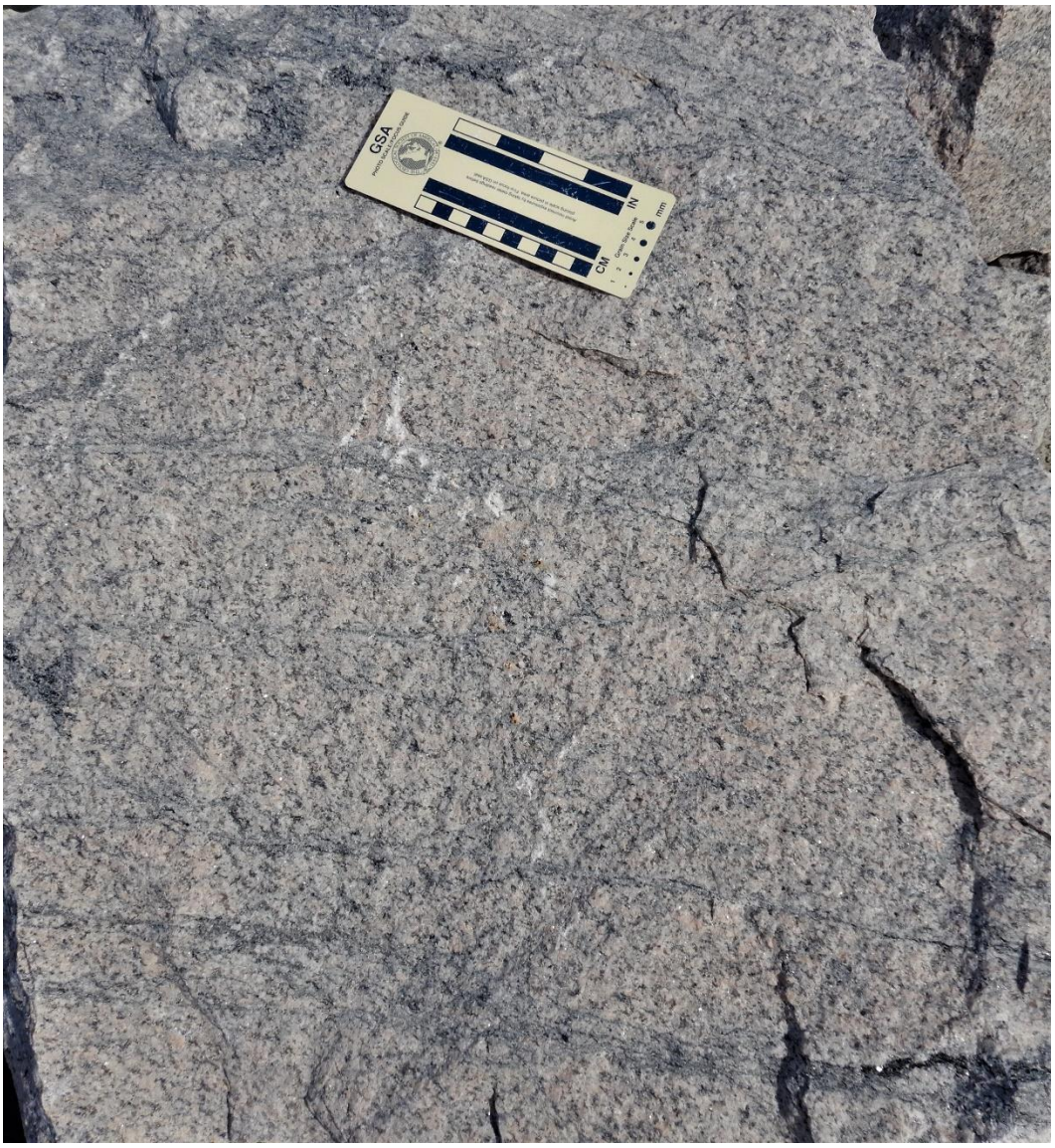

Fig. 8. Flow brecciation of main granitic phase at Hanson Quarry.

Fig. 9. Biotite-rich shear zone in main phase of granite at Hanson Quarry. Note sigmoidal shear sense indicators.

Fig. 10. Aplite dike with diffuse contact with main granitic phase. A xenolith can be observed on the lower right (Hanson Quarry).

Fig. 11. Pegmatite vein with smoky quartz core and diffuse contact with main phase (Hanson Quarry)

Fig. 12. Aplite and pegmatite phase with high proportions of smoky quartz and microcline (Hanson Quarry).

Fig. 13. Pegmatite dikes crosscutting biotite shear zone.

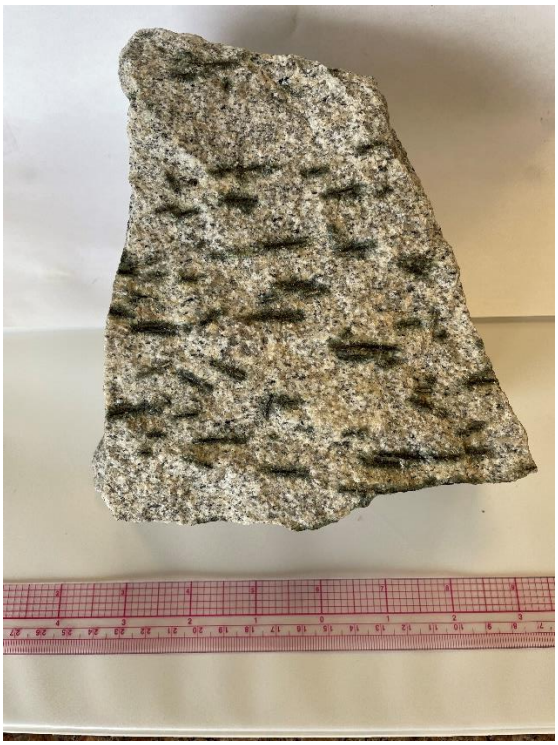

Fig. 14. Allanite crystals showing flow alignment in granite from Martin Marietta Quarry.

Fig. 15. Saprolite from Hanson Quarry with kaolin-rich zone above it. Note preserved granite texture in saprolite.

METHODS

A total of 23 thin sections were created from 17 different samples using Grindstone Laboratories located in Portland, OR. The thin sections all had a thickness of 30 microns and standard dimensions of 27 mm by 46 mm, embedded in EPO-Tek 301 epoxy and mounted with Loctite 363 adhesive with a glass cover slip. The samples and sample locations are detailed in Appendix Table 1. Thin sections were analyzed using a Leica DM750P Petrographic Microscope and a 1 mm mechanical stage. Photomicrographs were taken with Leica Application Suite v4.9. Geochemical data was acquired for representative samples through whole rock geochemical analysis performed by Actlabs LTD located in Ontario, Canada. Major and trace element data was acquired using inductively coupled plasma mass spectrometry (ICP-MS) according to the 4Litho package listed on Actlabs' website (https://actlabs.com). The quality of the data is compared to numerous standards to ensure high precision.

RESULTS

Petrography

For the main granitic phase, major minerals from all three quarries included quartz, microcline, plagioclase, and biotite. Quartz and microcline were the dominant minerals and appeared in roughly equal proportions for the main phase granite. Grain size of major minerals was highly variable throughout all samples and can be classified as seriate. Quartz grains were consistently the largest, followed by microcline and then plagioclase. Occasional large (>5 mm) grains of microcline were observed, but these were more typically associated with pegmatitic phases. The main granite was typically hypidiomorphic to allotriomorphic, with euhedral crystals occurring rarely. Grain boundaries were often irregular and sutured (Fig. 16). Quartz appeared as an intergrowth in microcline, but not in high enough proportions to consider the rock granophyric.

Major mineral distribution was more variable for the aplites. The aplites possessed a higher proportion of quartz and microcline with significantly less plagioclase at the Vulcan Quarry, whereas the Hanson Quarry aplites possessed more variable amounts of quartz and microcline but always a higher proportion of plagioclase. Biotite was almost always missing from the aplites, except in some cases where biotite grains are aligned as foliated stringers. The aplites were all allotriomorphic granular with very fine (<.25 mm) grains. Plagioclase grains showed a faint alignment that suggested a trachytoidal texture. Grain boundaries were straight and showed little to no signs of stress. Alteration and deformation features observed in the main phase granite were generally absent from the aplites. While the aplites that were analyzed typically came from dikes, aplitic material was also found as small pockets appearing in the main phase granite. These aplite pockets were usually observed near diffuse contacts between pegmatite-aplite dikes and the main granitic phase but also occasionally as isolated occurrences.

Plagioclase frequently showed albite and Carlsbad twinning as well as compositional zoning, while microcline typically had a well-developed perthitic texture. Plagioclase composition is in the oligoclase to albite range. Sericite alteration was extensively prevalent in the feldspars, particularly plagioclase. Due to the preferential sericitization of plagioclase, perthitic microcline and albite twinning were often observable in plane polarized light. Microcline often had tartan twinning in large grains. Deformation features were prevalent

throughout the main phase granite. Large deformation cracks spanning multiple grains were frequent, typically filled with goethite, highly birefringent sericite, chlorite, or rarely carbonate minerals. Quartz had undulose extinction and fracturing present in nearly all grains. Plagioclase grains were often broken and healed, demonstrating extensive irregular fractures filled with goethite or sericite (Fig. 17). Bending of albite twin traces in plagioclase also demonstrated deformation effects. Myrmekite was frequently embedded in microcline grains in samples from the Vulcan Quarry.

An amphibole mineral, likely hornblende, was present in small quantities in samples from the Vulcan quarry and much more frequently in samples from the Hanson quarry. Hornblende grains were typically irregular in size and shape but distinguished by inclined extinction and cleavage traces. Biotite was present in most samples, ranging from euhedral elongate laths to irregular crystals. Chlorite alteration was significant for biotite, with some crystals completely altered. Most biotite was regularly interspersed in the main phase granite, but occasional biotite-amphibole stringers were observed. Epidote is present both as a secondary alteration mineral and as a primary mineral. Aggregates of hornblende, biotite, epidote, and opaque minerals are common throughout many samples from the Hanson Quarry. Several pegmatite-aplite samples contained subhedral garnet as a minor mineral. The garnets ranged in size from around 0.5 mm to ~1 cm and displayed fractures and strain indictors. Two large garnet crystals contained concentrated aggregates of opaque minerals.

Accessory minerals were present among all three quarries, but in different proportions and in different phases. Opaque minerals were fairly ubiquitous in most phases but generally absent from the aplites. These opaques were often cubic in form and possessed goethite or hematite rims, indicating an iron-bearing sulfide or oxide mineral such as pyrite or magnetite. Apatite was also present among most phases as long needle-like crystals with high relief and was frequently associated with biotite. Fine, highly birefringent zircon crystals were present throughout the main granitic phase and frequently as inclusions in other minerals. Allanite crystals were present with a range of sizes, from fine inclusions to large, macroscopic grains as seen in Fig. 14. Allanite displayed varying degrees of metamictization, with radial cracks extending from larger crystals as well as zoned cores (Fig. 18). Sphene was found primarily in samples from the Vulcan Quarry, either as subhedral to euhedral crystals or smaller inclusions.

Apatite, zircon, and allanite were all nearly or completely absent from the pegmatite-aplite phase. Monazite and/or xenotime may have been present, but these crystals were extraordinarily small and can frequently be confused with zircon. Finally, anhedral fluorite was present in the pegmatite-aplite phase, identified by its distinct octahedral cleavage traces and isotropic nature.

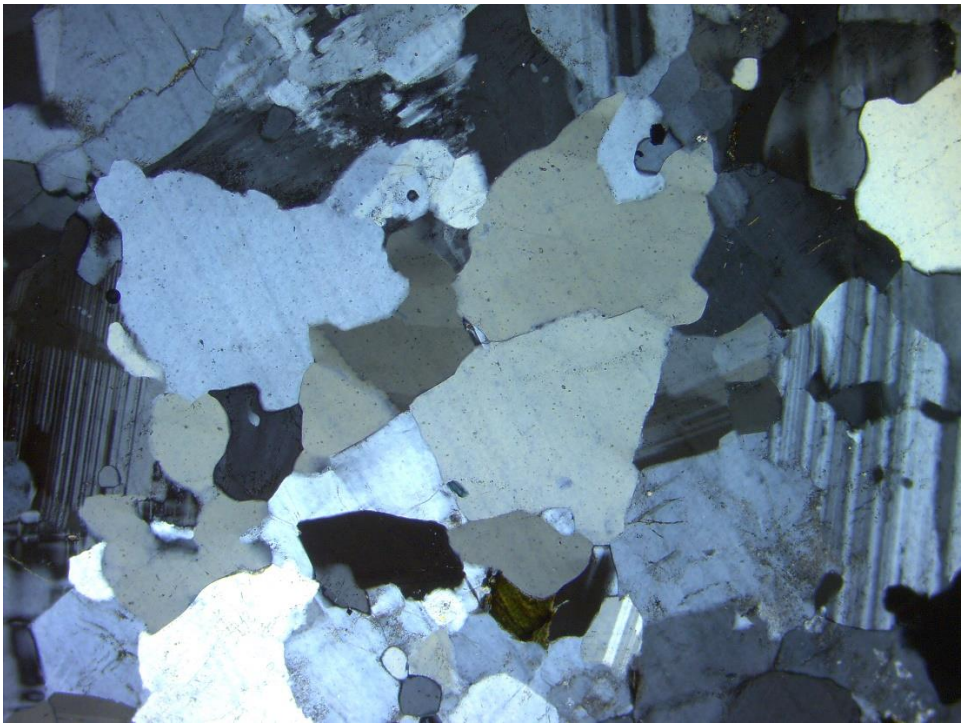

Fig. 16. Hypidiomorphic seriate texture of main phase granite with sutured grain boundaries (50x magnification, XPL).

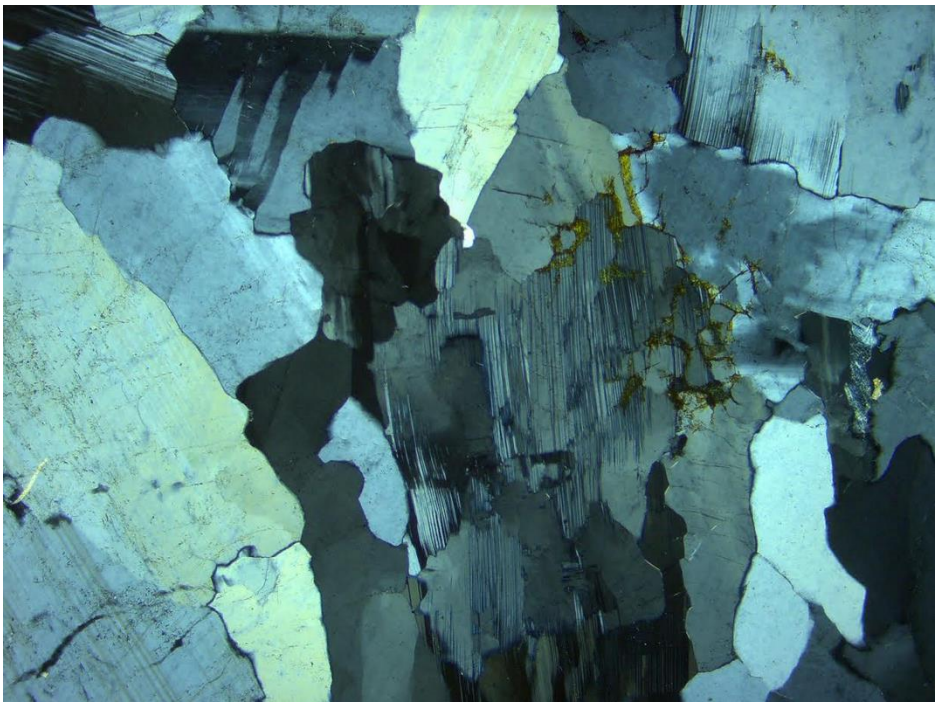

Fig. 17. Deformation and alteration in main phase granite. Note brecciation of plagioclase (50x magnification, XPL).

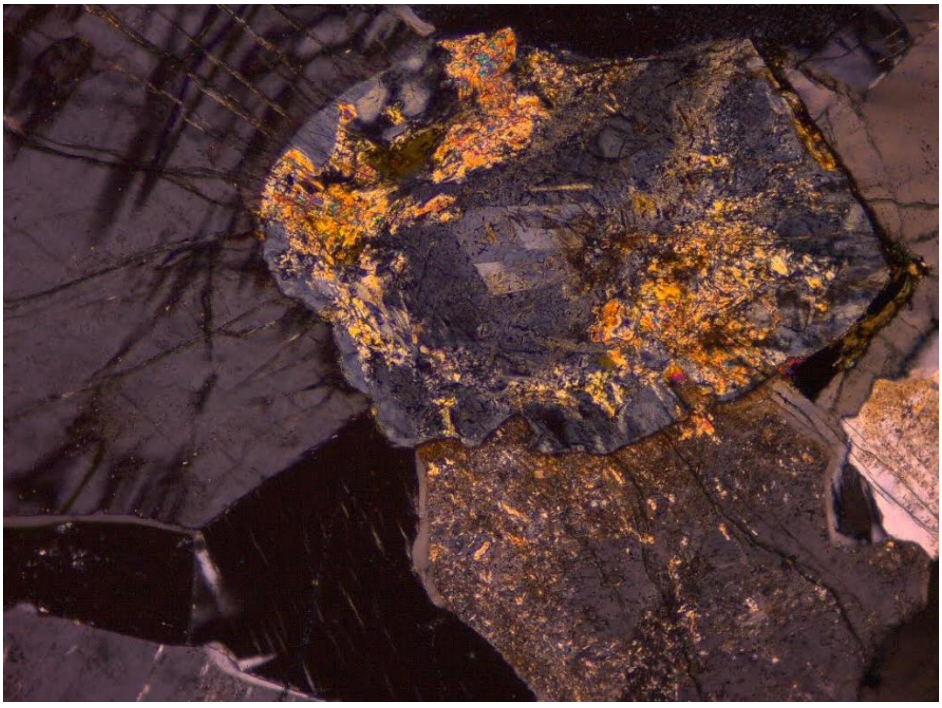

Fig. 18. Partially metamict allanite with radial expansion cracks and epidote alteration (100x magnification, XPL).

Modal Analysis

Point counts were performed on 18 thin sections; several sections were omitted from point counts due to their coarse grain size preventing them from being suitable representative samples. Results of point counts can be seen in Appendix Table 2. All granitic main phase samples can be classified as true granites; monzogranite is the dominant classification among all three quarries, with only two samples classified as syenogranites (Fig. 19). The aplites from the Hanson quarry have highly variable classifications but are more abundant in plagioclase than the main granite phase, as seen by the samples classified as granodiorites and quartz monzodiorite. Conversely, the aplites from the Vulcan quarry possess a greater abundance of microcline than most of the main granite samples, suggesting that the Vulcan aplites are more closely genetically related to the pegmatite phase than the Hanson aplites.

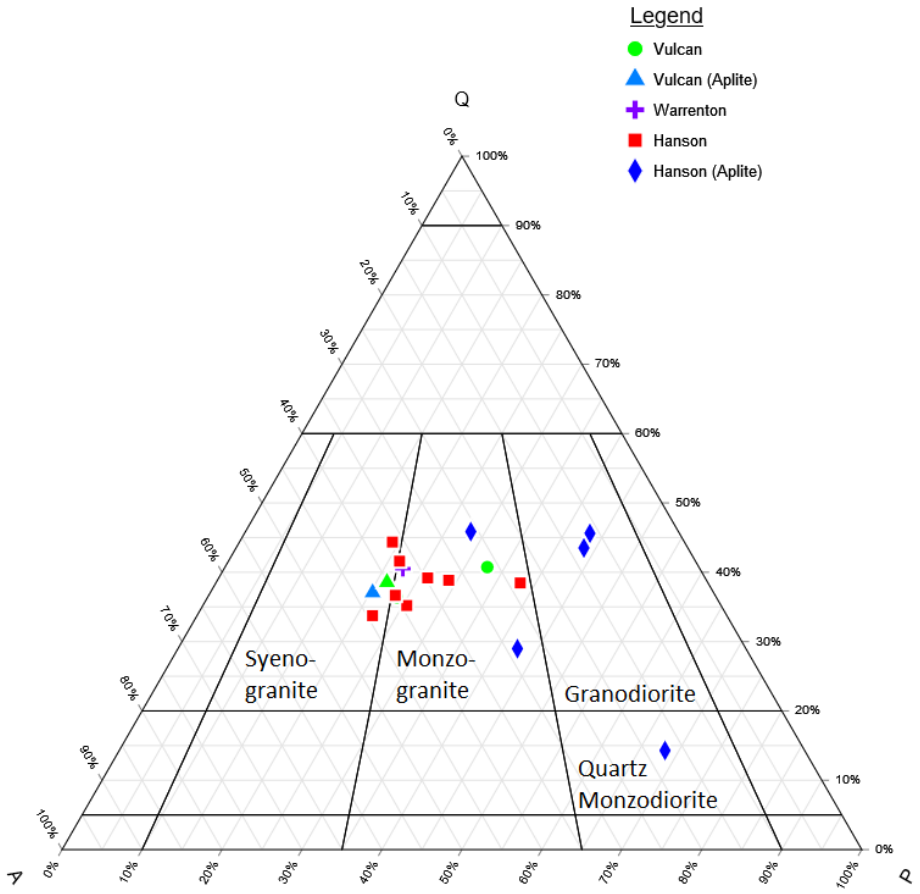

Fig. 19. Modal abundance of quartz, plagioclase, and alkali feldspar plotted on a QAP diagram to determine granitoid rock classification (Streckeisen, 1974).

Geochemistry

The major and trace element data for various samples are presented in Appendix Table 3. Geochemical data was acquired mainly from representative main phase granite samples from the Vulcan Quarry (BH-13 through BH-25), with two aplite samples (BH-1C and BH-10B). One pegmatite-aplite sample from the Hanson Quarry (HPA-1) and three representative main phase granite samples from the Martin Marietta Quarry (MW-4A, MW-4B, and FV-2A) were also analyzed.

Bivariate diagrams were generated by plotting various elements and element oxides against silica (Fig. 20-31). Lower silica content is generally accepted as being representative of a more primitive phase, while higher silica content is indicative of a more fractionated, younger phase. The aplite and pegmatite-aplite samples all plotted with high amounts of silica, suggesting that they were highly fractionated phases. Al_2O_3 decreases steeply with increasing silica content, which may be due in part to lower proportions of feldspars to quartz, but also to a decrease in biotite content. Fe2O3, MgO, MnO, and TiO_2 content decreases as silica content increases, indicating lower amounts of mafic minerals in more evolved phases. CaO decreases steadily with more evolved phases and may be due to the development of more sodic plagioclase in later stages. Na_2O remains steady throughout. The expected trend would be an increase in Na_2O in the later phases as plagioclase content increases; there is a sharp increase in Na_2O content with the pegmatite-aplite sample, but additional aplite samples would be necessary to confirm this positive trend. K_2O content peaks towards the center of silica content distribution, which could be explained by an increased presence of microcline in later main phase granite but an absence in the aplite phase. P_2O_5 and Zr follow similar negatively sloping trends, and can likely be explained by a lack of apatite and zircon in the most fractionated phases, respectively.

A general decrease in LREE content, as demonstrated by La + Ce, can be observed. This is likely attributed to the high LREE content in allanite, which is missing from later phases. A less pronounced decrease of HREE can be observed, as demonstrated by Yb + Lu. This is likely due to a lack of zircon in later phases. One exception, however, is the HREE content of the Hanson pegmatite-aplite sample, which contains more HREE than any other sample; this may be attributed to the presence of a significant amount of garnet and a lack of other REE-bearing accessory phases.

The Shand Alumina Saturation Index (ASI) can be determined using the formula $ASI = \frac{Al_2O_3}{(Na_2O+K_2O+CaO)}$. These values range from 1.34 to 1.46, meaning the rocks are strongly peraluminous (Fig. 32). A strongly peraluminous nature is characteristic of an S-type granite, which is supported for the Sparta complex by the presence of biotite and garnet. This is at odds with the 0.7035 Sr^{87}/Sr^{86} ratio reported by Fullagar and Butler (1976), which suggests that there was almost no assimilation of a supracrustal sedimentary source typical of an S-type granite. Using the Modified Alkali-Lime Index (MALI), the main phase granite samples plot primarily in the calc-alkalic range and partially in the alkali-calcic range (Peacock, 1931). The aplites are calc-alkalic, bordering on alkali-calcic.

The normal mid-ocean ridge basalt (N-MORB) normalized major element plots (Fig. 34) shows an enrichment of large ion lithophile elements (LILE), a dip in Ta, Nb, P, and Ti. The patterns are consistent for all the samples, though the aplite-containing samples show a greater depletion of Sr, Ba, and most high field strength elements (HFSE). The chondrite normalized REE plots demonstrated a relative enrichment of LREE that is higher than that of the HREE (Fig. 35). The exceptions to this are BH-10B, an aplite, and HPA-1, a pegmatite-aplite. A large negative Eu anomaly can be seen for most samples, likely due to substitution of divalent Eu for calcium in plagioclase and amphibole in the source rock, depleting the more fractionated magma. Samples with a slightly positive Eu anomaly or none may be influenced by the REE content of accessory minerals that crystallized early in the crystallization process and not from the more depleted magma.

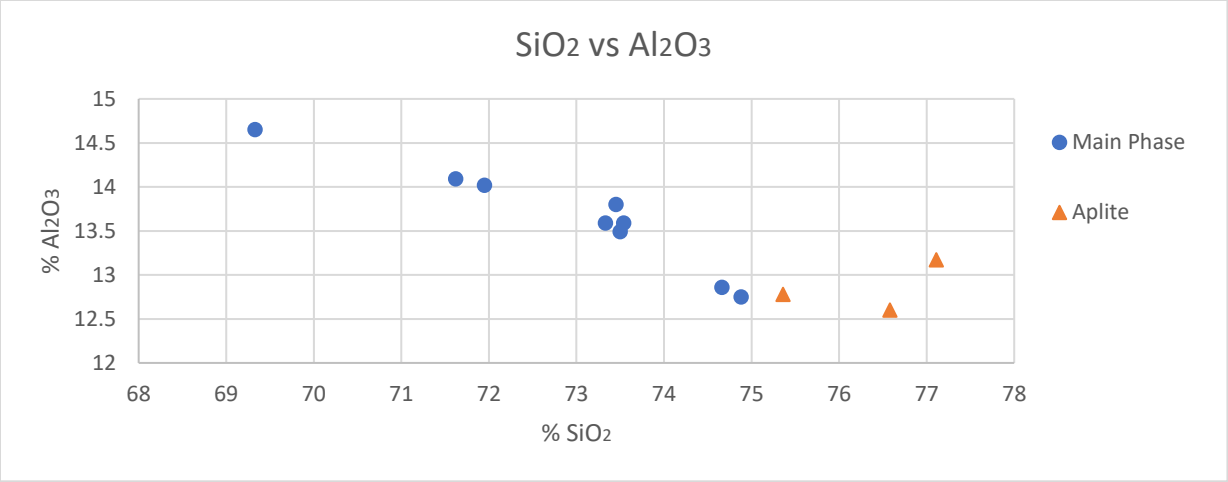

Fig. 20. Graph of SiO_2 vs Al_2O_3.

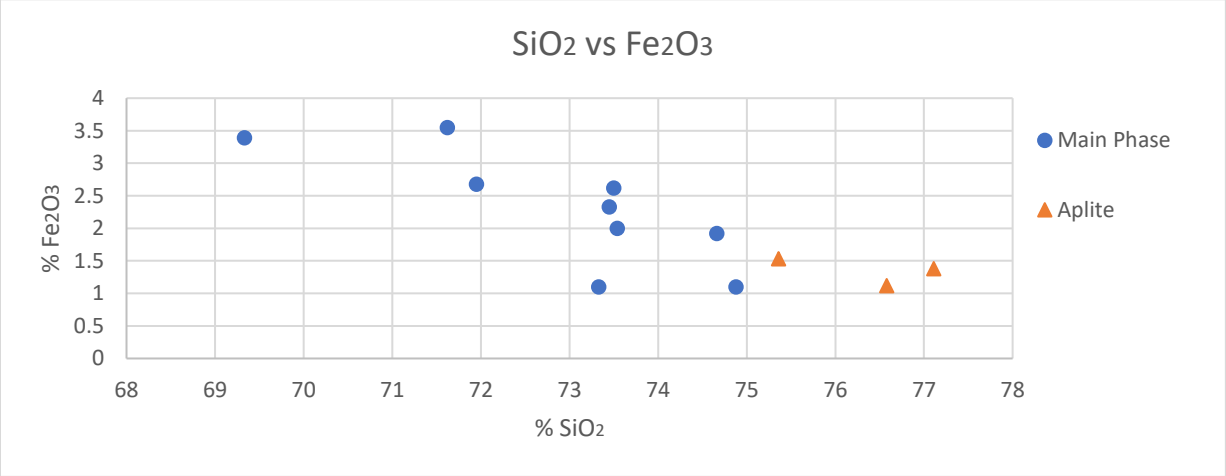

Fig. 21. Graph of SiO_2 vs Fe_2O_3.

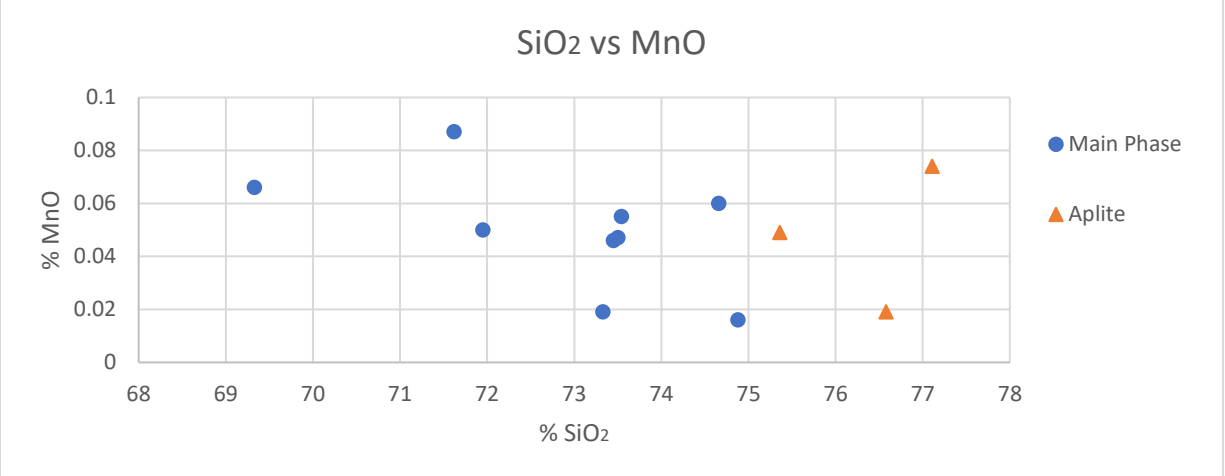

Fig. 22. Graph of SiO_2 vs MnO.

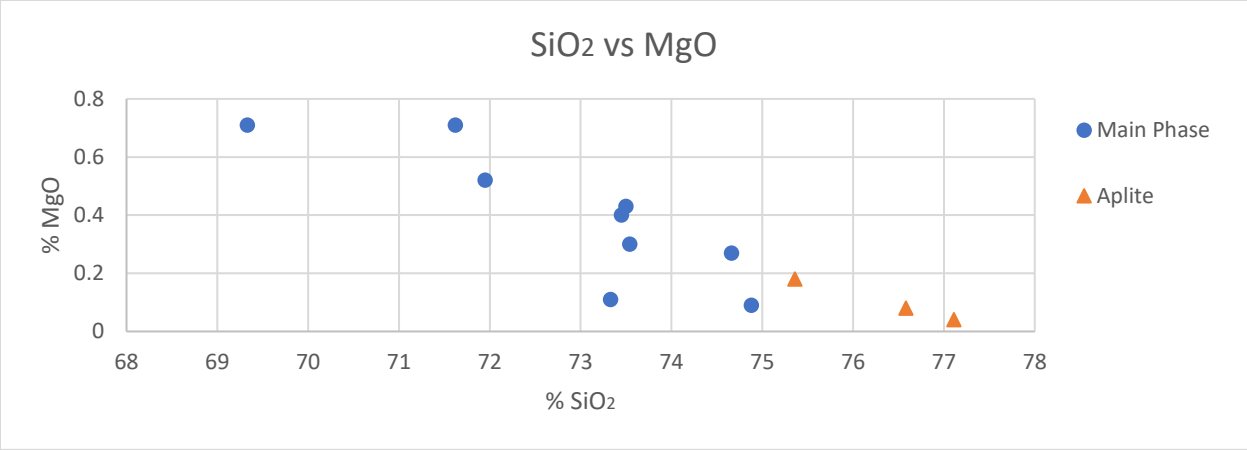

Fig. 23. Graph of SiO_2 vs MgO.

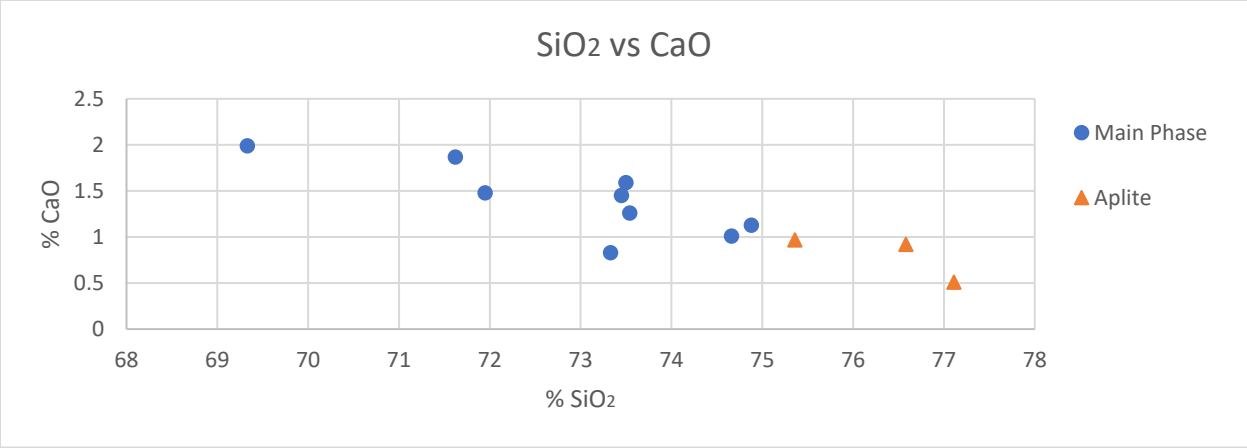

Fig. 24. Graph of SiO_2 vs CaO.

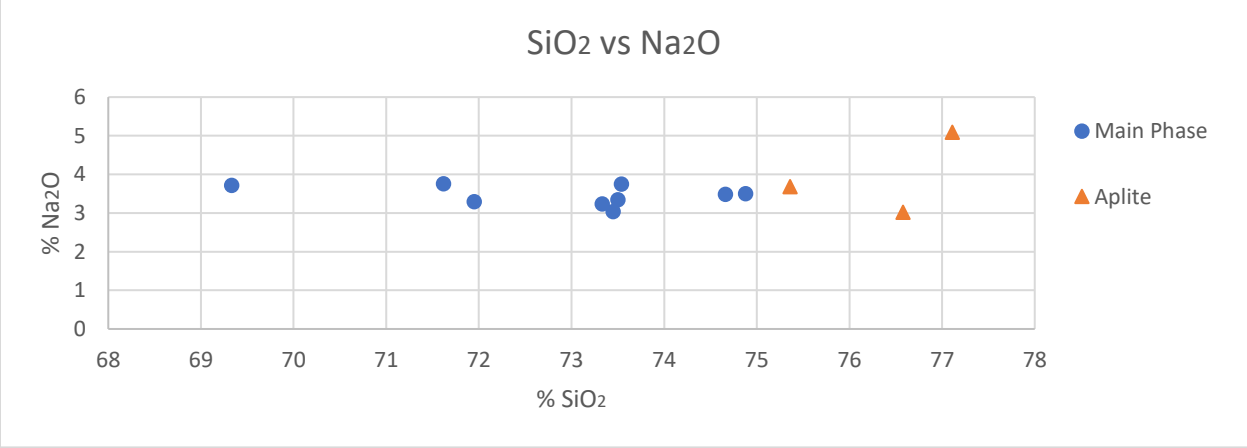

Fig. 25. Graph of SiO_2 vs Na_2O.

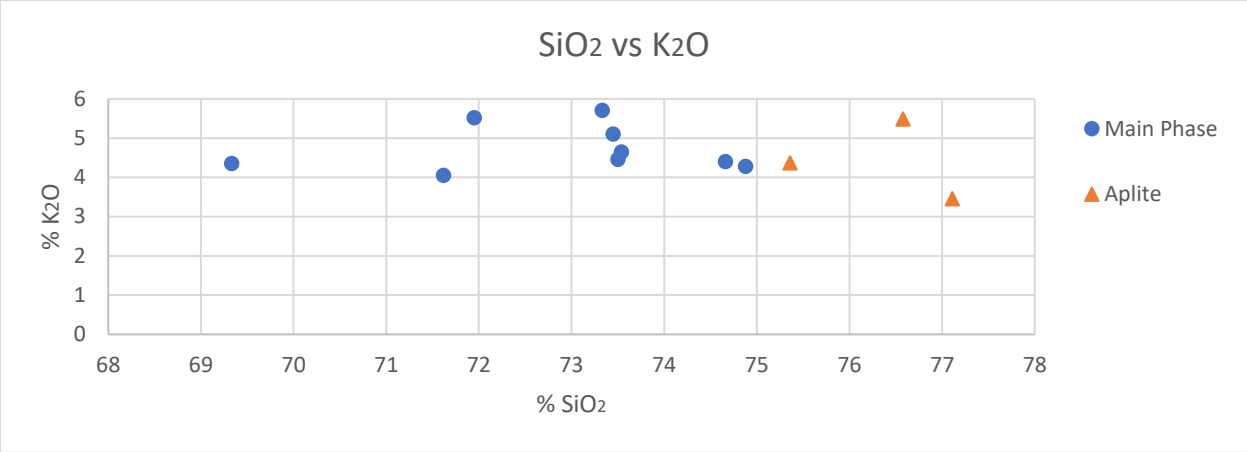

Fig. 26. Graph of SiO_2 vs K_2O.

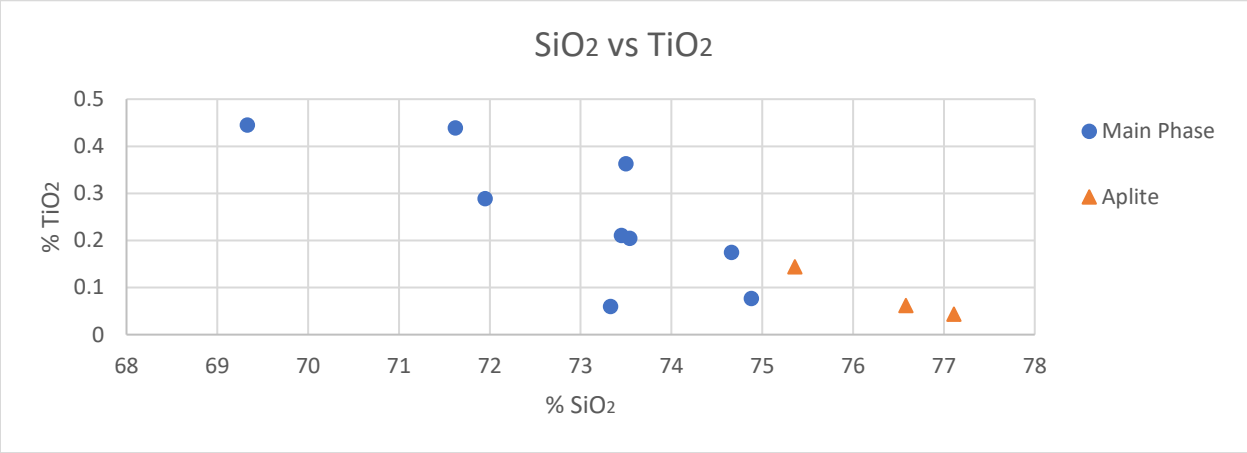

Fig. 27. Graph of SiO_2 vs TiO_2.

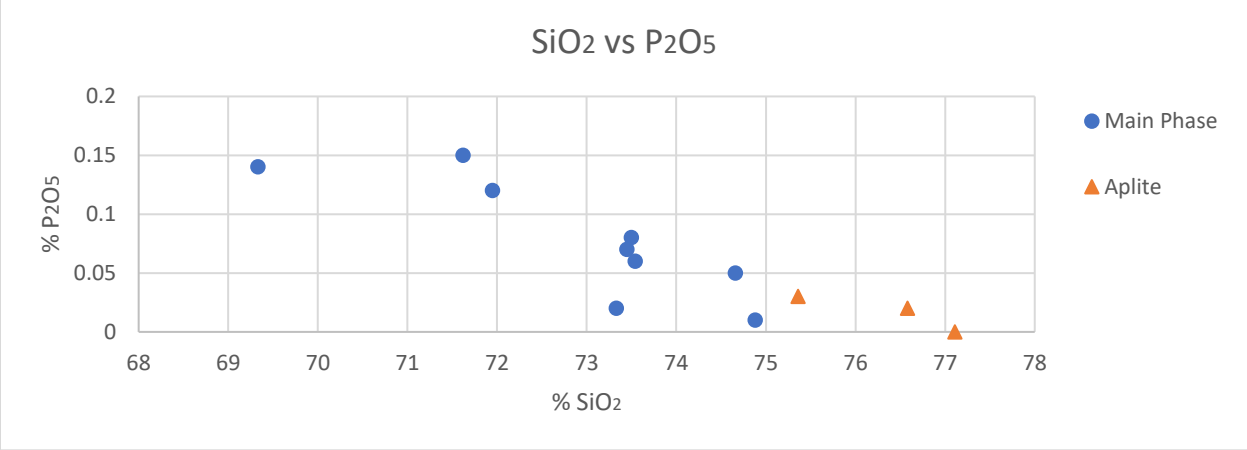

Fig. 28. Graph of SiO_2 vs P_2O_5.

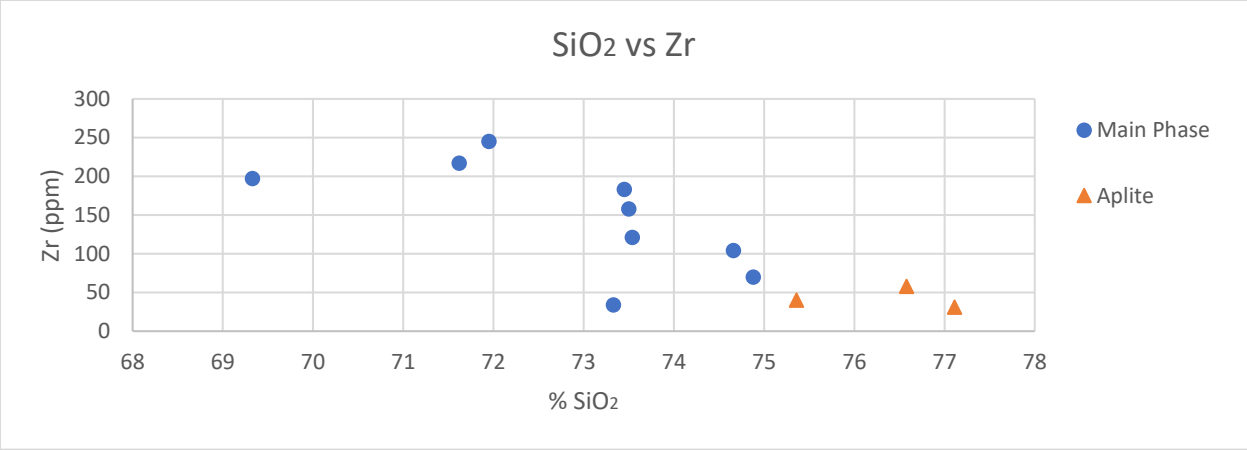

Fig. 29. Graph of SiO_2 vs Zr.

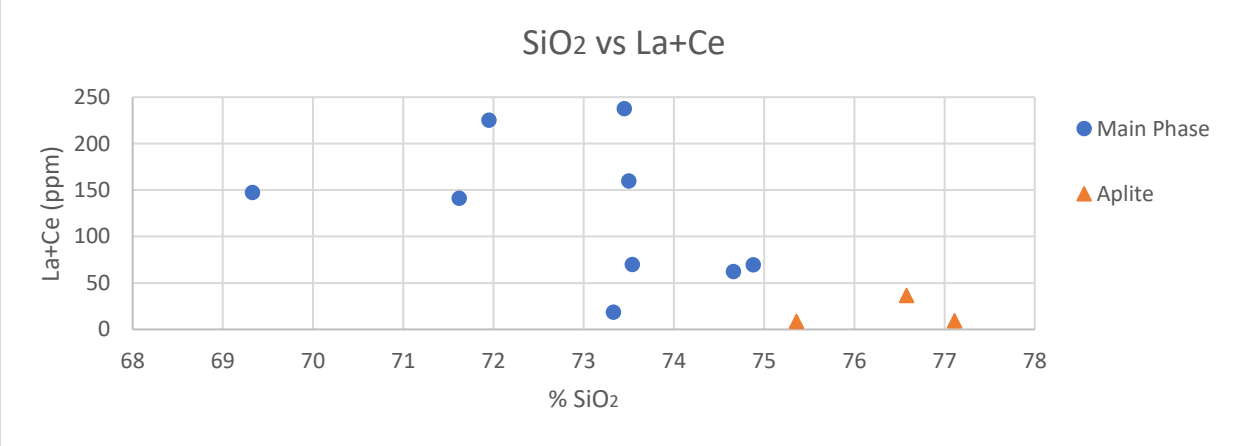

Fig. 30. Graph of SiO_2 vs La+Ce.

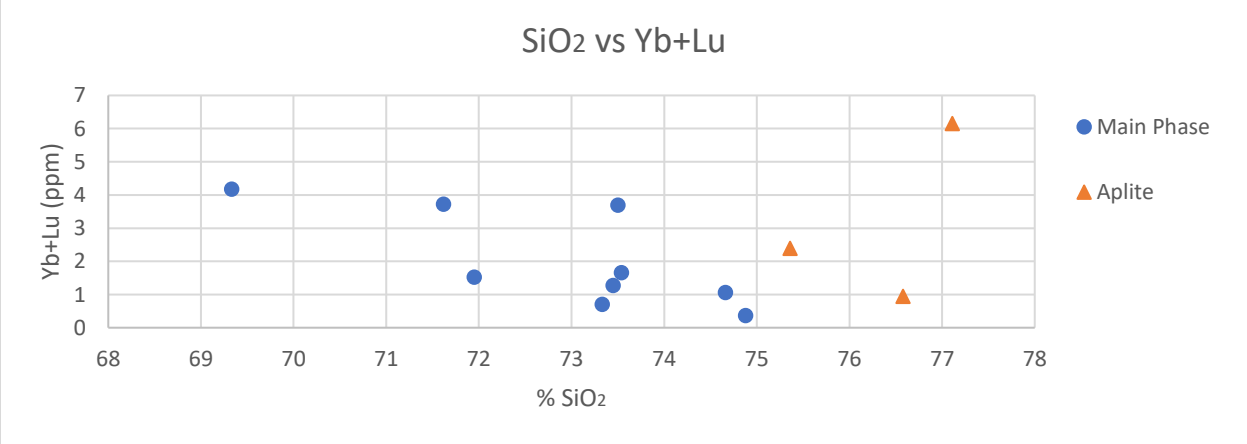

Fig. 31. Graph of SiO_2 vs Yb+Lu.

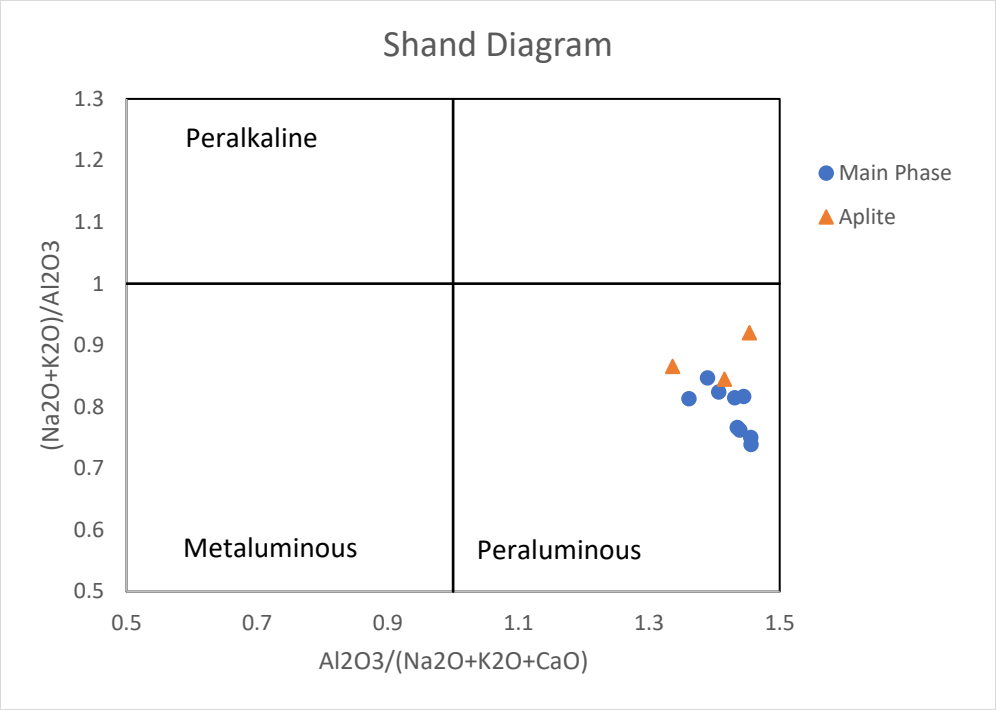

Fig. 32. Diagram of Shand alumina classification to show relative molar proportions of alumina vs alkali content (Shand, 1943).

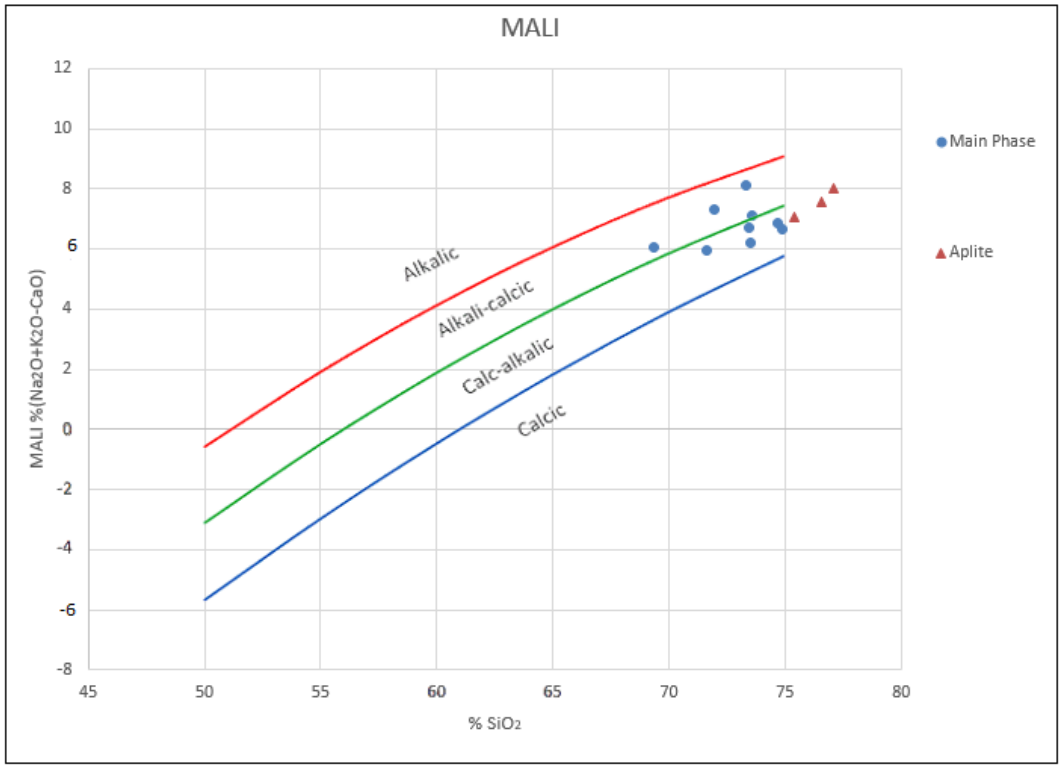

Fig. 33. Modified Alkali Lime Index (MALI) plotted against SiO_2 wt % (Peacock, 1931).

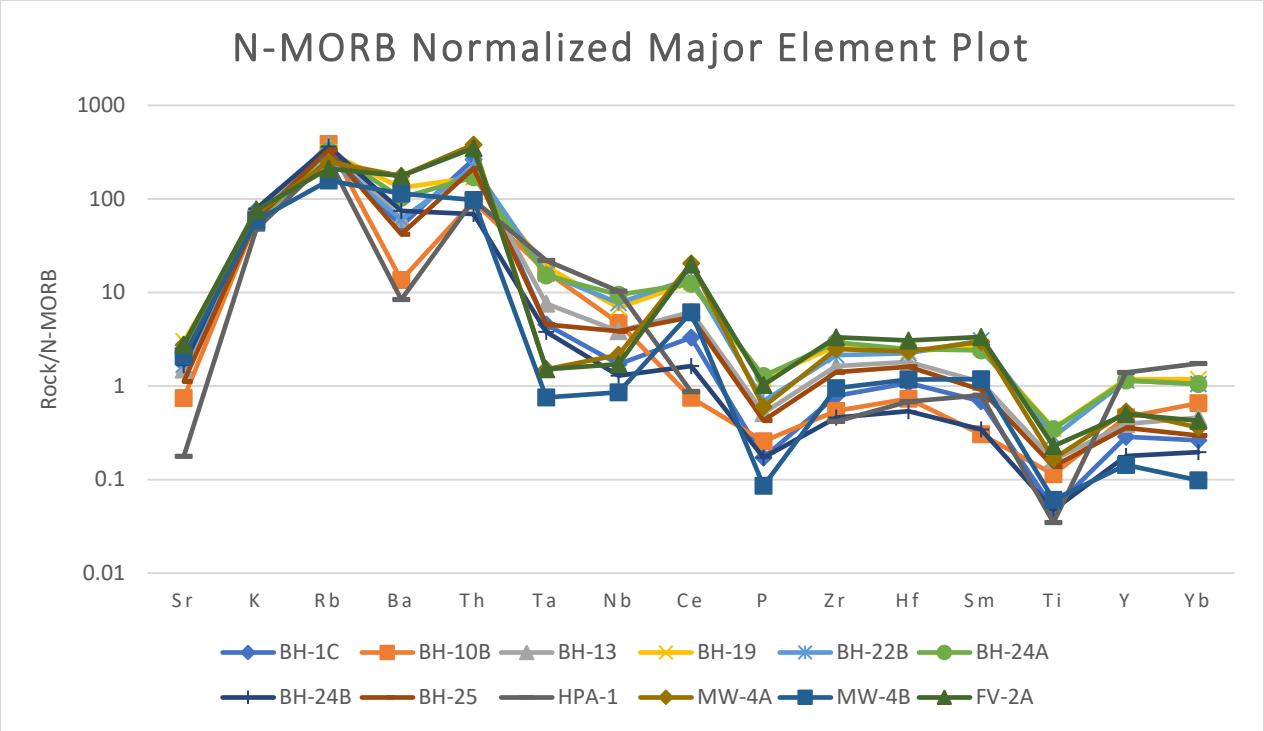

Fig. 34. N-MORB normalized plot of major elements.

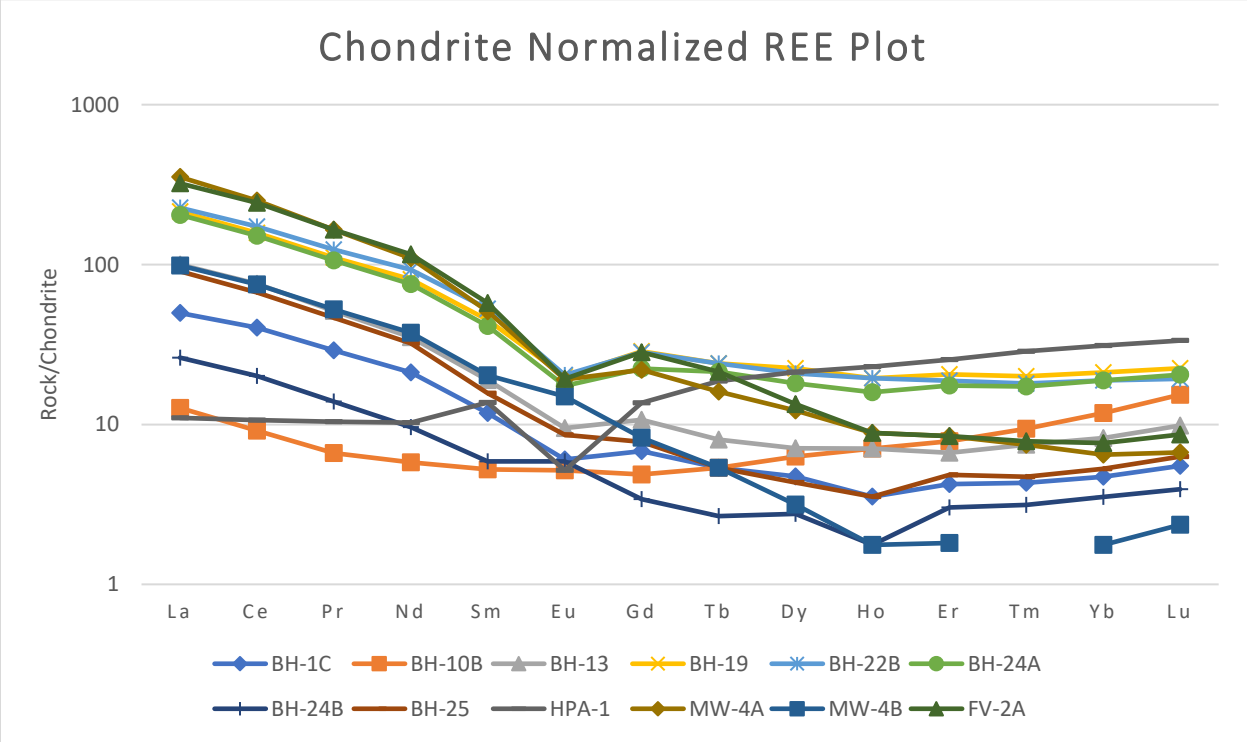

Fig. 35. Chondrite-normalized plot of REE.

DISCUSSION

Tectonic Discrimination

The N-MORB normalized major element plot patterns are most similar to that of volcanic arc basalts due to the enrichment of LILE and the dip in Ta and Nb (Fig. 35). However, the HFSE pattern is not as flat as would be typically expected of a purely volcanic arc granite (Winter, 2001). The dip in P content and enrichment of Ce could be due to crustal assimilation, which is also logical due to the relative enrichment of Rb and Th over Ta and Nb. A large negative Ba anomaly can also be characteristic of crustal assimilation, as well as high amounts of fractional crystallization (Pearce et al., 1984). The negative Eu anomaly present in most samples (Fig. 36) supports the idea of a more fractionated melt as opposed to a high amount of crustal assimilation.

Tectonic discrimination plots based on Pearce et al. (1984) were also created. The plot of Y vs. Nb (Fig. 36) shows the samples plotting primarily in the volcanic arc/syn collisional granite range, with a few samples plotting as ocean ridge granites with anomalous ridge sediments. The plots of Yb vs. Ta (Fig. 37) and Nb + Y (Fig. 38) show samples plotting primarily as volcanic arc granites, with some on the border of syn collisional and within plate settings. These findings align with the results of the N-MORB major element plot and support the idea for a granite originating from an oceanic volcanic arc. As the Sparta granite complex is known to have been emplaced in the Carolina zone, which contains multiple volcanic arc terranes, this origin aligns with its regional setting. The presence of biotite and hornblende as ferromagnesian minerals, classification as syeno/monzo-granite, and Peacock classification as calc-alkaline suggest specifically a high K calc-alkaline and shoshonitic active continental margin origin (Pearce et al., 1984).

The reason for the wide spread of samples on the Pearce et al. (1984) tectonic discrimination diagrams may be due to several problems of application listed in the work. Notably, aplite samples are not ideal for this sort of plot. Additionally, more samples would be ideal for a more accurate tectonic discrimination due to the wide range of textures present in the Sparta granite. Beyond limitations based on texture, hydrothermal alteration may play a role in skewing results, particularly sericitization and chloritization, both of which were observed extensively in Sparta granite samples.

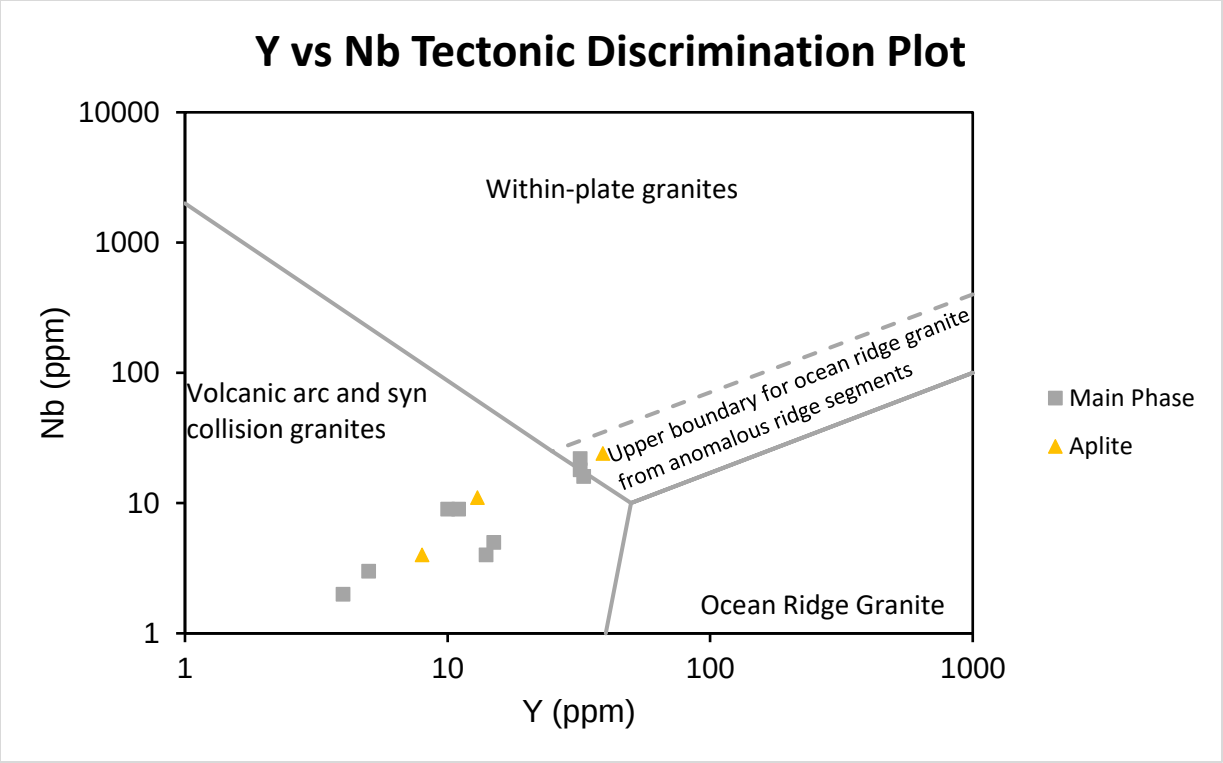

Fig. 36. Y vs Nb tectonic discrimination plot (Pearce et al., 1984).

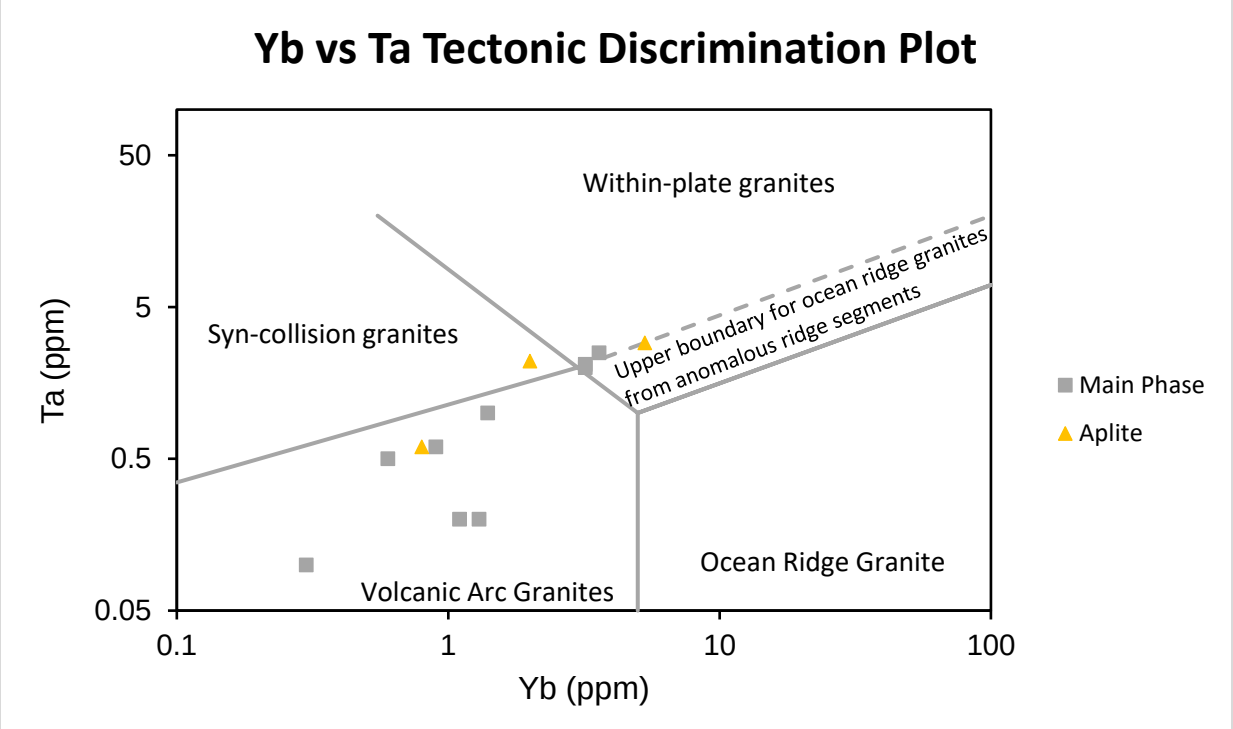

Fig. 37. Yb vs Ta tectonic discrimination plot (Pearce et al., 1984).

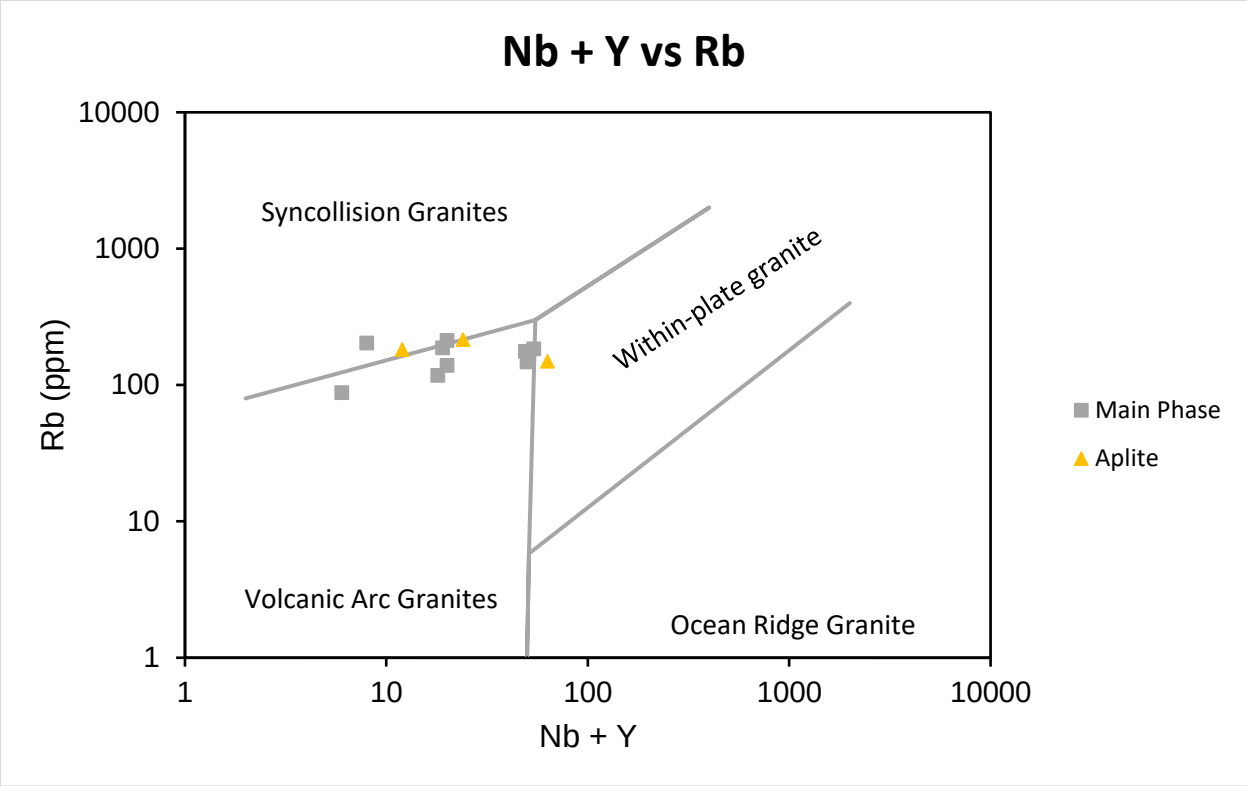

Fig. 38. Nb + Y vs Rb tectonic discrimination plot (Pearce et al., 1984).

Petrogenesis

Unlike most granitoid plutons, the Sparta granite complex contains a variety of phases with differing compositions and textures on both an outcrop and regional level. This wide range of phases is likely due to an extensive sequence of fractional crystallization and even perhaps multiple injections of magma. Modal amounts of quartz, microcline, and plagioclase tend to vary between main granitic phases and aplite-pegmatite phases, with aplites containing a much higher proportion of plagioclase. Biotite and hornblende were present almost exclusively in the main granitic phases, but varied regionally between different quarries, with some locales completely lacking in hornblende. Additionally, the Hanson Quarry showed much less variation in main phase granite texture than the other two quarries.

Accessory mineral content was also highly variable, with zircon, allanite, and apatite observed in main granitic phases while garnet was more often present in the pegmatites. At the Martin Marietta Quarry, allanite was occasionally present as large euhedral crystals, suggesting an early crystallization in a more primitive phase. Sphene was observed in all phases, but less so

in the pegmatite-aplite samples. The presence of biotite in the main phase granite may have promoted the crystallization of apatite and zircon, as boundary layer enrichment of biotite during crystallization can lead to an increased presence of those accessory minerals (Clarke et al., 2021). This is supported by the identification of apatite and zircon inclusions in biotite.

Alteration was significant throughout the main phase granitic phases, typically in the form of sericite on feldspars and chloritization of biotite. This alteration was fairly advanced, and some crystals were almost fully altered, indicating a long period of alteration. Due to the presence of extensive alteration on fresh samples, it can be reasoned that alteration occurred due to autometasomatism from late stage magmatic fluid rather than penetration of meteoric water. This is also supported by the presence of fluorite, which is typically associated with hydrothermal activity.

Structural features throughout the granite indicate either a tectonic or more local force was exerting stress on the pluton throughout some portion of the crystallization process. The main granitic phase demonstrates the presence of myrmekite, sutured grain boundaries, and deformation cracks on a microscopic level, while flow brecciation and shear zones are seen macroscopically. These stressors may have been due to multiple injections of magma into the magma chamber, late-stage tectonic activity from the Alleghanian orogeny and nearby Modoc Shear Zone, or some combination of the two. It is more likely that stress was due to multiple magma injections, as there is little to no deformation present in the late stage pegmatite-aplite phase.

Pegmatites and aplites were often associated with each other and crosscut all other phases, indicating they formed last and at relatively the same time. The aplites may have formed slightly later than the pegmatites, as they tend to appear more as “pockets” in the pegmatites and main phase granite. This is also indicated by the lack of microcline in most of the aplites, suggesting a Na-rich residual melt formed after the crystallization of microcline in the pegmatites. There is also a relative lack of accessory minerals in the aplites versus the main phase granite and pegmatites.

Rare-Earth Element Potential

Due to a lack of data from residual overburden material, it is difficult to make direct observations about REE potential of the Sparta granite complex. However, some predictions can be made based on the mineralogy and weathering conditions of the granite. By evaluating felsic partition coefficients (K_d) it is possible to determine what minerals are responsible for REE content in various phases (Appendix Table 5). Accessory minerals have K_d values for REEs that are orders of magnitude higher than what is typical for rock forming minerals and are thus highly interesting for the development of economic-grade residual deposits.

The main granitic phase contained high amounts of LREE (Fig. 30), Zr (Fig. 29), and P_2O_5 (Fig. 28). This supports the idea that more fractionated phases had lower amounts of allanite, zircon, and apatite respectively. The phosphate contribution may have also been due to the presence of xenotime, but this is likely negligible when compared to the amount of apatite in the rock. This mineralogical distribution is supported by thin section observations of these minerals, particularly for allanite, which was observed in unusually large quantities. Allanite was likely responsible for the high LREE content seen in Fig. 35, as it has extraordinarily high K_d values for LREE. Zircon likely accounted for main phase HREE content, as granite was typically absent. Apatite may have provided an overall higher REE content for this phase, as its K_d values are more even across the element series.

The pegmatite-aplite samples tended to have less LREE content and sometimes more HREE than LREE. While zircon has high K_d values for HREE, it was likely garnet that contributed the overall HREE content. A lack of apatite and sphene may have also contributed to the seemingly higher HREE content, as these accessory phases were not present to increase the overall REE content and balance out the distribution.

CONCLUSIONS

The rocks of the Sparta granite complex are strongly peraluminous (Fig. 32) calc-alkaline to alkali-calcic (Fig. 33) syeno-granites and monzo-granites (Fig. 19). N-MORB normalized major element plots (Fig. 34) and tectonic discrimination diagrams (Fig. 36-38) suggest an oceanic volcanic arc origin, with some possible assimilation of crustal material. These results are consistent with previous interpretations on the origin of the complex (Fullagar and Butler, 1976; Speer et al., 1994) but suggest that crustal contamination may be more significant or complicated than previously thought.

The Sparta granite complex is highly fractionated and contains several different phases and structural features that suggest multiple magma injections were involved in its emplacement. Residual melt and volatiles were responsible for extensive alteration across the main granitic phase. There may have been additional influence from the nearby Modoc shear zone that contributed to early deformation in the complex, but a lack of any metamorphic texture suggests this was limited. The pegmatite and aplite phase were the last to crystallize as they are free of deformation and alteration signs.

REE-bearing accessory phases were present throughout the complex but varied in distribution between phases and across the region. Garnet was likely responsible for HREE content in the pegmatite-aplite phase, while zircon is responsible for main phase HREE. Allanite, apatite, and sphene account for LREE in the main phase. Apatite and zircon associate commonly with biotite, which was particularly concentrated in certain main phase textures (Clarke et al., 2021).

Overall, the Sparta granite complex has significant REE potential. All the phases contain the necessary accessory minerals for REE content, with different phases contributing to LREE and HREE enrichment in different proportions. Alteration of the main granitic phase may have contributed to the formation of secondary minerals that could increase the mobility of REEs in a weathering profile. Residual deposits above the complex have not been evaluated geochemically but are several meters thick and possess the conditions for precipitation and dissolution mediated REE mobility. Future work should evaluate the geochemistry of the overlying residual material and examine which portions of the soil horizon are most enriched in REE, as well as how secondary clay minerals contribute to REE mobility.

ACKNOWLEDGEMENTS

Thank you to the Semratedu Undergraduate Research Fund for funding portions of this project as well as Vulcan Materials Company, Hanson Aggregates, and Martin Marietta Aggregates for allowing us to collect samples. Thank you to Grindstone Laboratories for their excellent thin section work. I would also like to thank Dr. Robert Kelly Vance for his invaluable expertise and mentorship over the course of this project, as well as all my peers at Georgia Southern University for their support.

REFERENCES CITED

Burton, J., 2022, National News Release: U.S. Geological Survey Releases 2022 List of Critical Minerals: https://www.usgs.gov/news/national-news-release/us-geological-survey-releases-2022-list-critical-minerals (Accessed January 2023)

Cheshire, M.C., Bish, D.L., Cahill, J.F., Kertesz, V., and Stack, A.G., 2018, Geochemical Evidence for Rare-Earth Element Mobilization during Kaolin Diagenesis: ACS Earth and Space Chemistry, vol. 2, issue 5, p. 506-520, doi:10.1021/acsearthspacechem.7b00124

Clarke, D. B., Renno, A.D., Hamilton, D.C., Gilbricht, S., and Bachmann, K., 2021, The spatial association of accessory minerals with biotite in granitic rocks from the South Mountain Batholith, Nova Scotia, Canada: Geosphere, v. 18, no. 1, p. 1–18, https://doi.org/10.1130/GES02339.1.

da Silva, Y.J.A.B., do Nascimento, C.W.A., Biondi, C.M., van Straaten, P., de Souza Junior, V.S., da Silva, Y.J.A.B., dos Santos, C.A., and de Araujo, J. do C.T., 2017, Influence of metaluminous granite mineralogy on the rare earth element geochemistry of rocks and soils along a climosequence in Brazil: Geoderma, v. 306, p. 28–39, doi:10.1016/j.geoderma.2017.06.031.

Fischer, E., Vance, R.K., Massey, S., 2020, A petrological study of the Sparta Granite, Warrenton Quarry, Georgia: Geological Society of America Abstracts with Programs, doi:10.1130/abs/2020SE-345316.

Foley, N., Ayuso, R., Hubbard, B., Bern, C., and Shah, A., 2015, Geochemical and Mineralogical Characteristics of REE in Granite-Derived Regolith of the Southeastern United States, in Proceeding of the 13th Biennial SGA Meeting, Nancy: Eastern Mineral and Environmental Resources Science Center, p. 725-728

Fullagar, P.D., Butler, J.R., 1976, Petrochemical and geochronologic studies of plutonic rocks in the southern Appalachians; II, The Sparta granite complex, Georgia: Geological Society of America Bulletin, v. 87, p. 53-56.

Hibbard, J.P., Stoddard, E.F., Secor, D.T., Dennis, A.J., 2002, The Carolina Zone: overview of Neoproterozoic to Early Paleozoic peri-Gondwanan terranes along the eastern Flank of the southern Appalachians: Earth-Science Reviews, v. 57, p. 299-339.

Jin, L., Ma, L., Dere, A., White, T., Mathur, R., and Brantley, S.L., 2017, REE mobility and fractionation during shale weathering along a climate gradient: Chemical Geology, v. 466, p. 352–379, doi:10.1016/j.chemgeo.2017.06.024.

Massey, S., and Vance, R.K., 2019, Petrology and petrography of granitoid intrusions in the Warrenton Quarry, GA: Geological Society of America Abstracts with Programs, doi:10.1130/abs/2019SE-327432.

Mukai, H., Kon, Y., Sanematsu, K., Takahashi, Y., and Ito, M., 2020, Microscopic analyses of weathered granite in ion adsorption rare earth deposit of Jianxi Province, China: Scientific Reports, v. 10, p. 1-11, doi:10.1038/s41598-020-76981-8.

Peacock, M.A., 1931, Classification of igneous rock series: Journal of Geology, v. 39, p. 54-67.

Pearce, J.A., Harris, N.B.W., and Tindle, A.G., 1984, Trace Element Discrimination Diagrams for the Tectonic Interpretation of Granitic Rocks: Journal of Petrology, v. 25, iss. 4, p. 956-983, doi:10.1093/petrology/25.4.956.

Precambrian Research Group: New Mexico Tech, 1989, Felsic Distribution Coefficients

Shand, S.J., 1943, The Eruptive Rocks, Second Edition: New York, John Wiley, 444 p.

Speer, J.A., McSween, H.Y., Gates, A.E., 1994, Generation, Segregation, Ascent, and Emplacement of Alleghanian Plutons in the Southern Appalachians: The Journal of Geology, v. 102, p. 249-267.

Streckeisen, A., 1974, Classification and nomenclature of plutonic rocks, recommendations of the IUGS subcommission on the systematics of igneous rocks: Geologische Rundschau, v. 63, p. 773-786, doi:10.1007/bf01820841

Whitney, J.A., and Wenner, D.B., 1980, Petrology and Structural Setting of Post-Metamorphic Granites of Georgia: Geological Society of America: Atlanta Guidebook, v. 93, p. 351-378.

Winter, J.D., 2001, Introduction to Igneous and Metamorphic Petrology, First Edition, Pearson College Div, 697 p.

Yang, M., Liang, X., Ma, L., Huang, J., He, H., and Zhu, J., 2019, Adsorption of REEs on kaolinite and halloysite: A link to the REE distribution on clays in the weathering crust of granite: Chemical Geology, v. 525, p. 210–217, doi:10.1016/j.chemgeo.2019.07.024.

Yusoff, Z.M., Ngwenya, B.T., and Parsons, I., 2013, Mobility and fractionation of REEs during deep weathering of geochemically contrasting granites in a tropical setting, Malaysia: Chemical Geology, v. 349–350, p. 71–86, doi:10.1016/j.chemgeo.2013.04.016.

APPENDIX

Table 1. Sample name and quarry location for thin sections. Labels in parentheses are alternate names used for geochemistry.

Sample Name	Source Quarry for Sample
MH1Aa	Hanson
MH1Ab	Hanson
MH1B	Hanson
MH1D	Hanson
MH1E	Hanson
MH1F	Hanson
MH1Ha	Hanson
MH1Hb	Hanson
MH2A	Hanson
MH2B	Hanson
MH2D	Hanson
MH2E	Hanson
MH2F	Hanson
BH1	Vulcan
BH2	Vulcan
BH3a	Vulcan
BH3b	Vulcan
BH3c	Vulcan
BH3d	Vulcan
BH4a	Vulcan

BH4b	Vulcan
FV-34 (FV-2A)	Martin-Marietta
VE-1 (HPA-1)	Hanson

Table 2. Point count data from thin sections. Mode is total number of points counted for that mineral, while % is the calculated percentage out of the total number of points counted.

Sample	Quartz		Microcline		Plagioclase		Biotite		Epidote		Opaques		Allanite		Zircon		Hornblende		Garnet		Fluorite	
	Mode	%	Mode	%	Mode	%	Mode	%	Mode	%	Mode	%	Mode	%	Mode	%	Mode	%	Mode	%	Mode	%
MH1Aa	83	33.2	109	43.6	54	21.6	0	0	2	0.8	1	0.4	0	0	0	0	1	0.4	0	0	0	0
MH1Ab	96	38.4	85	34	64	25.6	5	2	0	0	0	0	0	0	0	0	0	0	0	0	0	0
MH1B	27	13.5	33	16.5	129	64.5	0	0	1	0.5	2	1	1	0.5	0	0	0	0	7	3.5	0	0
MH1D	88	35.2	96	38.4	56	22.4	6	2.4	1	0.4	3	1.2	0	0	0	0	0	0	0	0	0	0
MH1E	71	28.4	70	28	104	41.6	1	0.4	0	0	4	1.6	0	0	0	0	0	0	0	0	0	0
MH1F	87	43.5	26	13	87	43.5	0	0	0	0	0	0	0	0	0	0	0	0	0	0	0	0
MH1Ha	102	40.8	84	33.6	44	17.6	15	6	0	0	2	0.8	0	0	2	0.8	0	0	0	0	1	0.4
MH1Hb	83	41.5	47	23.5	51	25.5	17	8.5	0	0	0	0	0	0	2	1	0	0	0	0	0	0
MH2A	101	40.4	90	36	52	20.8	5	2	0	0	2	0.8	0	0	0	0	0	0	0	0	0	0
MH2B	94	37.6	78	31.2	70	28	2	0.8	4	1.6	0	0	0	0	1	0.4	1	0.4	0	0	0	0
MH2D	114	45.6	28	11.2	108	43.2	0	0	0	0	0	0	0	0	0	0	0	0	0	0	0	0
MH2E	87	34.8	97	38.8	63	25.2	2	0.8	0	0	1	0.4	0	0	0	0	0	0	0	0	0	0
BH1	74	37	77	38.5	41	20.5	7	3.5	0	0	1	0.5	0	0	0	0	0	0	0	0	0	0
BH3a	72	36	79	39.5	47	23.5	1	0.5	0	0	1	0.5	0	0	0	0	0	0	0	0	0	0
BH3c	73	36.5	84	42	40	20	3	1.5	0	0	0	0	0	0	0	0	0	0	0	0	0	0
BH4b	77	38.5	50	25	62	31	8	4	0	0	3	1.5	0	0	0	0	0	0	0	0	0	0
FV-34	96	38.4	88	35.2	53	21.2	4	1.6	6	2.4	2	0.8	1	0.4	0	0	0	0	0	0	0	0
VE-1	95	38	58	23.2	94	37.6	1	0.4	0	0	1	0.4	0	0	0	0	0	0	0	0	1	0.4

Table 3. Geochemical data obtained from Actlabs.

Analyte Symbol	SiO2	Al2O3	Fe2O3(T)	MnO	MgO	CaO	Na2O	K2O	TiO2	P2O5	LOI	Total
Unit Symbol	%	%	%	%	%	%	%	%	%	%	%	%
Detection Limit	0.01	0.01	0.01	0.005	0.01	0.01	0.01	0.01	0.001	0.01		0.01
Analysis Method	FUS-ICP	FUS-ICP	FUS-ICP	FUS-ICP	FUS-ICP	FUS-ICP	FUS-ICP	FUS-ICP	FUS-ICP	FUS-ICP	GRAV	FUS-ICP
BH-1C	76.58	12.6	1.12	0.019	0.08	0.92	3.02	5.49	0.062	0.02	0.25	100.2
BH-10B	75.36	12.78	1.53	0.049	0.18	0.97	3.69	4.37	0.144	0.03	0.23	99.32
BH-13	73.54	13.59	2	0.055	0.3	1.26	3.75	4.65	0.205	0.06	0.19	99.59
BH-19	69.33	14.65	3.39	0.066	0.71	1.99	3.72	4.35	0.445	0.14	0.42	99.2
BH-22B	73.5	13.49	2.62	0.047	0.43	1.59	3.35	4.46	0.363	0.08	0.36	100.3
BH-24A	71.62	14.09	3.55	0.087	0.71	1.87	3.76	4.05	0.439	0.15	0.51	100.8
BH-24B	73.33	13.59	1.1	0.019	0.11	0.83	3.24	5.71	0.06	0.02	0.32	98.33
BH-25	74.66	12.86	1.92	0.06	0.27	1.01	3.49	4.4	0.175	0.05	0.18	99.07
HPA-1	77.11	13.17	1.38	0.074	0.04	0.51	5.09	3.46	0.044	< 0.01	0.06	100.9
MW-4A	73.45	13.8	2.33	0.046	0.4	1.45	3.04	5.1	0.211	0.07	0.5	100.4
MW-4B	74.88	12.75	1.1	0.016	0.09	1.13	3.5	4.28	0.077	0.01	0.27	98.11
FV-2A	71.95	14.02	2.68	0.05	0.52	1.48	3.3	5.52	0.289	0.12	0.34	100.3

Analyte Symbol	Sc	Be	V	Ba	Sr	Y	Zr	Cr	Co	Ni	Cu	Zn
Unit Symbol	ppm	ppm	ppm	ppm	ppm	ppm	ppm	ppm	ppm	ppm	ppm	ppm
Detection Limit	1	1	5	2	2	1	2	20	1	20	10	30
Analysis Method	FUS-ICP	FUS-ICP	FUS-ICP	FUS-ICP	FUS-ICP	FUS-ICP	FUS-ICP	FUS-MS	FUS-MS	FUS-MS	JS-MS	FUS-MS
BH-1C	1	2	11	325	155	8	58	< 20	1	< 20	< 10	< 30
BH-10B	4	6	10	86	67	13	40	< 20	1	< 20	< 10	< 30
BH-13	4	5	16	387	135	11	121	< 20	2	< 20	< 10	< 30
BH-19	6	4	35	829	270	33	197	< 20	5	< 20	< 10	50
BH-22B	4	3	14	380	152	32	158	< 20	2	< 20	< 10	50
BH-24A	7	4	33	649	207	32	217	< 20	4	< 20	20	70
BH-24B	1	3	8	471	150	5	34	< 20	1	< 20	< 10	< 30
BH-25	4	4	13	265	101	10	104	< 20	2	< 20	< 10	50
HPA-1	6	10	< 5	53	16	39	31	< 20	< 1	< 20	< 10	50
MW-4A	3	2	19	1105	247	15	183	< 20	2	< 20	< 10	40
MW-4B	1	2	5	719	187	4	70	< 20	< 1	< 20	< 10	< 30
FV-2A	4	2	24	1107	249	14	245	< 20	2	< 20	< 10	40

Analyte Symbol	Ga	Ge	As	Rb	Nb	Mo	Ag	In	Sn	Sb	Cs	La
Unit Symbol	ppm	ppm	ppm	ppm	ppm	ppm	ppm	ppm	ppm	ppm	ppm	ppm
Detection Limit	1	1	5	2	1	2	0.5	0.2	1	0.5	0.5	0.1
Analysis Method	FUS-MS	FUS-MS	FUS-MS	FUS-MS	FUS-MS	FUS-MS	FUS-MS	FUS-MS	FUS-MS	FUS-MS	JS-MS	FUS-MS
BH-1C	13	1	< 5	182	4	< 2	< 0.5	< 0.2	1	< 0.5	2.8	11.8
BH-10B	18	2	< 5	216	11	< 2	< 0.5	< 0.2	1	< 0.5	5.8	3
BH-13	16	2	< 5	212	9	< 2	< 0.5	< 0.2	1	< 0.5	4.1	23.7
BH-19	17	1	< 5	177	16	< 2	< 0.5	< 0.2	2	< 0.5	5	50.8
BH-22B	16	1	< 5	148	18	2	< 0.5	< 0.2	2	< 0.5	3.1	53.7
BH-24A	17	2	< 5	184	22	< 2	< 0.5	< 0.2	3	< 0.5	5.6	48.5
BH-24B	14	1	< 5	203	3	< 2	< 0.5	< 0.2	< 1	< 0.5	3.2	6.2
BH-25	16	2	< 5	187	9	< 2	< 0.5	< 0.2	2	< 0.5	3.5	21.5
HPA-1	22	3	< 5	149	24	< 2	< 0.5	< 0.2	5	< 0.5	2.8	2.6
MW-4A	14	1	< 5	139	5	2	< 0.5	< 0.2	1	< 0.5	1.2	83.6
MW-4B	12	1	< 5	88	2	3	< 0.5	< 0.2	1	< 0.5	0.7	23.4
FV-2A	14	1	< 5	118	4	< 2	< 0.5	< 0.2	1	< 0.5	1.7	76.3

Analyte Symbol	Ce	Pr	Nd	Sm	Eu	Gd	Tb	Dy	Ho	Er	Tm	Yb
Unit Symbol	ppm	ppm	ppm	ppm	ppm	ppm	ppm	ppm	ppm	ppm	ppm	ppm
Detection Limit	0.1	0.05	0.1	0.1	0.05	0.1	0.1	0.1	0.1	0.1	0.05	0.1
Analysis Method	FUS-MS	FUS-MS	FUS-MS	FUS-MS	FUS-MS	FUS-MS	FUS-MS	FUS-MS	FUS-MS	FUS-MS	JS-MS	FUS-MS
BH-1C	24.7	2.76	9.9	1.8	0.35	1.4	0.2	1.2	0.2	0.7	0.11	0.8
BH-10B	5.6	0.63	2.7	0.8	0.3	1	0.2	1.6	0.4	1.3	0.24	2
BH-13	46.3	4.86	16.4	2.9	0.55	2.2	0.3	1.8	0.4	1.1	0.19	1.4
BH-19	96.6	10.5	37.8	6.9	1.16	5.9	0.9	5.7	1.1	3.4	0.51	3.6
BH-22B	106	11.8	43.3	8.1	1.18	5.8	0.9	5.3	1.1	3.1	0.46	3.2
BH-24A	92.6	10.1	35.2	6.3	1.01	4.6	0.8	4.6	0.9	2.9	0.44	3.2
BH-24B	12.3	1.32	4.5	0.9	0.34	0.7	0.1	0.7	0.1	0.5	0.08	0.6
BH-25	40.9	4.42	15	2.4	0.5	1.6	0.2	1.1	0.2	0.8	0.12	0.9
HPA-1	6.5	0.99	4.8	2.1	0.3	2.8	0.7	5.4	1.3	4.2	0.73	5.3
MW-4A	154	15.7	51.1	7.8	1.11	4.5	0.6	3.1	0.5	1.4	0.19	1.1
MW-4B	46	4.98	17.5	3.1	0.87	1.7	0.2	0.8	0.1	0.3	< 0.05	0.3
FV-2A	149	15.7	54.2	8.8	1.12	5.8	0.8	3.4	0.5	1.4	0.2	1.3

Analyte Symbol	Lu	Hf	Ta	W	Tl	Pb	Bi	Th	U
Unit Symbol	ppm	ppm	ppm	ppm	ppm	ppm	ppm	ppm	ppm
Detection Limit	0.01	0.2	0.1	1	0.1	5	0.4	0.1	0.1
Analysis Method	FUS-MS	FUS-MS	FUS-MS	FUS-MS	FUS-MS	FUS-MS	FUS-MS	FUS-MS	FUS-MS
BH-1C	0.14	2.2	0.6	< 1	0.9	32	< 0.4	31.9	3.4
BH-10B	0.39	1.5	2.2	< 1	1	36	< 0.4	11.3	8.8
BH-13	0.25	3.7	1	< 1	1	32	< 0.4	25	8.7
BH-19	0.57	4.8	2.5	< 1	0.9	24	< 0.4	20.4	5.7
BH-22B	0.49	4.6	2.1	2	0.8	22	< 0.4	26.6	5.1
BH-24A	0.52	5.1	2	< 1	1	24	< 0.4	20.4	4.4
BH-24B	0.1	1.1	0.5	< 1	1	36	< 0.4	8.3	4.4
BH-25	0.16	3.3	0.6	< 1	1	32	< 0.4	25.5	7.7
HPA-1	0.85	1.4	2.9	< 1	0.7	27	< 0.4	11.7	41.9
MW-4A	0.17	4.8	0.2	< 1	0.7	27	< 0.4	45.7	1.5
MW-4B	0.06	2.4	0.1	< 1	0.5	27	< 0.4	11.7	1
FV-2A	0.22	6.3	0.2	< 1	0.6	22	< 0.4	42	1.9

Table 4. Quality control standards used by Actlabs to ensure precision in data.

Analyte Symbol	SiO2	Al2O3	Fe2O3(T)	MnO	CaO	Na2O	K2O	TiO2	Ba	Sr	Zr	Cr	Co	Ni
Unit Symbol	%	%	%	%	%	%	%	%	ppm	ppm	ppm	ppm	ppm	ppm
Detection Limit	0.01	0.01	0.01	0.005	0.01	0.01	0.01	0.001	2	2	2	20	1	20
Analysis Method	FUS-ICP	FUS-ICP	FUS-ICP	FUS-ICP	FUS-ICP	FUS-ICP	FUS-ICP	FUS-ICP	FUS-ICP	FUS-ICP	FUS-ICP	FUS-MS	FUS-MS	FUS-MS
NIST 694 Meas	10.47	1.82	0.78	0.012	42.93	0.86	0.53	0.111						
NIST 694 Cert	11.2	1.8	0.79	0.0116	43.6	0.86	0.51	0.11						
GBW 07113 Meas	69.25	12.73	3.22	0.137	0.59	2.46	5.34	0.287	504	42	392			
GBW 07113 Cert	72.8	13	3.21	0.14	0.59	2.57	5.43	0.3	506	43	403			
SY-4 Meas	50	20.11	6.05	0.103	7.89	6.95	1.66	0.291	346	1191	523			
SY-4 Cert	49.9	20.69	6.21	0.108	8.05	7.1	1.66	0.287	340	1191	517			
BIR-1a Meas	48.26	15.51	11.05	0.166	13.39	1.83	0.03	0.983	7	109	16	390	50	170
BIR-1a Cert	47.96	15.5	11.3	0.175	13.3	1.82	0.03	0.96	6	110	18	370	52	170
ZW-C Meas												60		
ZW-C Cert												56		
OREAS 101b (Fusion) Meas													44	< 20
OREAS 101b (Fusion) Cert													47	9
NCS DC86318 Meas														
NCS DC86318 Cert														
USZ 25-2006 Meas														70
USZ 25-2006 Cert														70.8
DNC-1a Meas	46.93	18.24	9.61	0.143	11.25	1.91	0.22	0.474	109	144	40			
DNC-1a Cert	47.15	18.34	9.97	0.15	11.49	1.89	0.234	0.48	118	144	38			
BCR-2 Meas	54.7	13.59	13.67	0.19	7.26	3.06	1.79	2.272	710	340	189			
BCR-2 Cert	54.1	13.5	13.8	0.196	7.12	3.16	1.79	2.26	683	346	188			
USZ 42-2006 Meas														
USZ 42-2006 Cert														
REE-1 Meas												290		20
REE-1 Cert												277		24.7
W-2b Meas	53.12	15.65	10.79	0.16	10.9	2.21	0.62	1.089	181	197	96	90	43	60
W-2b Cert	52.4	15.4	10.7	0.163	10.9	2.14	0.626	1.06	182	190	94	92	43	70
HPA-1 Orig	77.27	13.1	1.37	0.073	0.51	5.08	3.45	0.044	53	16	31	< 20	< 1	< 20
HPA-1 Dup	76.96	13.23	1.38	0.074	0.5	5.11	3.47	0.043	53	16	31	< 20	< 1	< 20
Method Blank												< 20	< 1	< 20
Method Blank	0.01	< 0.01	0.01	< 0.005	0.01	< 0.01	< 0.01	< 0.001	< 2	< 2	< 2			
Method Blank	0.01	< 0.01	< 0.01	< 0.005	< 0.01	< 0.01	< 0.01	< 0.001	< 2	< 2	< 2			

Analyte Symbol	Cu	Zn	Ga	Ge	As	Rb	Nb	Mo	Ag	In	Sn	Sb	Cs	La
Unit Symbol	ppm	ppm	ppm	ppm	ppm	ppm	ppm	ppm	ppm	ppm	ppm	ppm	ppm	ppm
Detection Limit	10	30	1	1	5	2	1	2	0.5	0.2	1	0.5	0.5	0.1
Analysis Method	FUS-MS	FUS-MS	FUS-MS	FUS-MS	FUS-MS	FUS-MS	FUS-MS	FUS-MS	FUS-MS	FUS-MS	FUS-MS	FUS-MS	FUS-MS	FUS-MS
NIST 694 Meas														
NIST 694 Cert														
GBW 07113 Meas														
GBW 07113 Cert														
SY-4 Meas														
SY-4 Cert														
BIR-1a Meas	120	70	15									0.5		0.7
BIR-1a Cert	125	70	16									0.58		0.63
ZW-C Meas		1090	90			> 1000	217				> 1000	4.6	265	29.6
ZW-C Cert		1050	99			8500	198				1300	4.2	260	30
OREAS 101b (Fusion) Meas	420							19						769
OREAS 101b (Fusion) Cert	420							21						789
NCS DC86318 Meas						383							11.3	1960
NCS DC86318 Cert						369.42							11.88	1960
USZ 25-2006 Meas		620												> 2000
USZ 25-2006 Cert		600												19300
DNC-1a Meas														
DNC-1a Cert														
BCR-2 Meas														
BCR-2 Cert														
USZ 42-2006 Meas		450			213		34	35						> 2000
USZ 42-2006 Cert		469			224		31	34.4						21100
REE-1 Meas	80					> 1000	> 1000				490		1.1	1700
REE-1 Cert	79.7					1050	4050				498		1.07	1661
W-2b Meas	110	80	17			19						0.8		10.8
W-2b Cert	110	80	17			21						0.79		10
HPA-1 Orig	< 10	40	22	3	< 5	146	23	< 2	< 0.5	< 0.2	4	< 0.5	2.7	2.5
HPA-1 Dup	< 10	50	22	3	< 5	151	24	< 2	< 0.5	< 0.2	5	< 0.5	2.9	2.6
Method Blank	< 10	< 30	< 1	< 1	< 5	< 2	< 1	< 2	< 0.5	< 0.2	< 1	< 0.5	< 0.5	< 0.1
Method Blank														
Method Blank														

Analyte Symbol	Ce	Pr	Nd	Sm	Eu	Gd	Tb	Dy	Ho	Er	Tm	Yb	Lu	Hf
Unit Symbol	ppm	ppm	ppm	ppm	ppm	ppm	ppm	ppm	ppm	ppm	ppm	ppm	ppm	ppm
Detection Limit	0.1	0.05	0.1	0.1	0.05	0.1	0.1	0.1	0.1	0.1	0.05	0.1	0.01	0.2
Analysis Method	FUS-MS	FUS-MS	FUS-MS	FUS-MS	FUS-MS	FUS-MS	FUS-MS	FUS-MS	FUS-MS	FUS-MS	FUS-MS	FUS-MS	FUS-MS	FUS-MS
NIST 694 Meas														
NIST 694 Cert														
GBW 07113 Meas														
GBW 07113 Cert														
SY-4 Meas														
SY-4 Cert														
BIR-1a Meas	2		2.5	1.1	0.54							1.7		0.6
BIR-1a Cert	1.9		2.5	1.1	0.55							1.7		0.6
ZW-C Meas	99.8	9.4	25	6.8		4.3			1.9		1.6	14.2	2.22	9.6
ZW-C Cert	97	9.5	25	6.6		4.7			2		1.6	14	2.2	9.7
OREAS 101b (Fusion) Meas	1310	123	375	48	7.56		5.1	30	6	17.8	2.57	16.7	2.48	
OREAS 101b (Fusion) Cert	1331	127	378	48	7.77		5.37	32.1	6.34	18.7	2.66	17.6	2.58	
NCS DC86318 Meas	410	724	> 2000	> 1000	18.9	> 1000	485	> 1000	598	> 1000	269	> 1000	257	
NCS DC86318 Cert	432	737	3429	1725	18.91	2168	468	3224	560	1750	271	1844	264	
USZ 25-2006 Meas	> 3000	> 1000		837	195							54.9		
USZ 25-2006 Cert	29000	2800		900	211							54.5		
DNC-1a Meas														
DNC-1a Cert														
BCR-2 Meas														
BCR-2 Cert														
USZ 42-2006 Meas	> 3000	> 1000	> 2000	496	83				7.7			18.3		
USZ 42-2006 Cert	27600	2300	6500	539	87.22				7.86			17.85		
REE-1 Meas	> 3000	438	1480	398	24.4	429	113	900	214	727	112	716		504
REE-1 Cert	3960	435	1456	381	23.5	433	106	847	208	701	106	678		479
W-2b Meas	23.4		13.3	3.5			0.6	3.9	0.8	2.3		2	0.33	2.6
W-2b Cert	23		13	3.3			0.63	3.6	0.76	2.5		2.1	0.33	2.6
HPA-1 Orig	6.3	0.99	4.6	2.1	0.3	2.8	0.7	5.4	1.2	4.1	0.71	5.2	0.85	1.3
HPA-1 Dup	6.6	0.99	5.1	2.2	0.3	2.8	0.7	5.5	1.3	4.3	0.74	5.5	0.85	1.5
Method Blank	< 0.1	< 0.05	< 0.1	< 0.1	< 0.05	< 0.1	< 0.1	< 0.1	< 0.1	< 0.1	< 0.05	< 0.1	< 0.01	< 0.2
Method Blank														
Method Blank														

Analyte Symbol	Ta	W	Tl	Pb	Bi	Th	U	MgO	P2O5	Total	Sc	Be	V	Y
Unit Symbol	ppm	ppm	ppm	ppm	ppm	ppm	ppm	%	%	%	ppm	ppm	ppm	ppm
Detection Limit	0.1	1	0.1	5	0.4	0.1	0.1	0.01	0.01	0.01	1	1	5	1
Analysis Method	FUS-MS	FUS-MS	FUS-MS	FUS-MS	FUS-MS	FUS-MS	FUS-MS	FUS-ICP	FUS-ICP	FUS-ICP	FUS-ICP	FUS-ICP	FUS-ICP	FUS-ICP
NIST 694 Meas								0.34	30.4				1690	
NIST 694 Cert								0.33	30.2				1740	
GBW 07113 Meas								0.15	0.05		5	4	< 5	46
GBW 07113 Cert								0.16	0.05		5	4	5	43
SY-4 Meas								0.52	0.13		< 1	3	6	123
SY-4 Cert								0.54	0.131		1.1	2.6	8	119
BIR-1a Meas								9.68	0.02		43	< 1	325	16
BIR-1a Cert								9.7	0.021		44	0.58	310	16
ZW-C Meas	80	317	33			45.4	19.5							
ZW-C Cert	82	320	34			43	20							
OREAS 101b (Fusion) Meas				< 5		36.2	391							
OREAS 101b (Fusion) Cert				20		37.1	396							
NCS DC86318 Meas						66								
NCS DC86318 Cert						67								
USZ 25-2006 Meas														
USZ 25-2006 Cert														
DNC-1a Meas								10.05	0.07		31		149	17
DNC-1a Cert								10.13	0.07		31		148	18
BCR-2 Meas								3.57	0.37		33		433	36
BCR-2 Cert								3.59	0.35		33		416	37
USZ 42-2006 Meas				1720		923								
USZ 42-2006 Cert				1600		946								
REE-1 Meas						746	143							
REE-1 Cert						719	137							
W-2b Meas						2.4	0.5	6.33	0.15		36	< 1	271	21
W-2b Cert						2.4	0.53	6.37	0.14		36	1.3	262	24
HPA-1 Orig	2.9	< 1	0.6	27	< 0.4	11.8	41.8	0.04	< 0.01	101	6	10	< 5	38
HPA-1 Dup	3	< 1	0.7	27	< 0.4	11.6	41.9	0.04	< 0.01	100.9	6	10	< 5	39
Method Blank	< 0.1	< 1	< 0.1	< 5	< 0.4	< 0.1	< 0.1							
Method Blank								< 0.01	< 0.01		< 1	< 1	< 5	< 1
Method Blank								< 0.01	0.02	0.06	< 1	< 1	< 5	< 1

Table 5. Felsic partition coefficients for select accessory minerals (Precambrian Research Group, 1989)

	Garnet	Zircon	Allanite	Apatite	Sphene
Rb	0.01	0	0	0	0
Sr	0.15	0	100	2	100
Cs	0.01	0	--	--	--
Ba	0.015	0	--	2	1
Th	0.02	100	1500	--	130
La	0.35	2	2500	20	32
Ce	0.35	2.5	2000	35	60
Nd	0.5	2.2	1700	57	180
Sm	2.6	3.1	1300	63	200
Eu	1	3.5	800	30	120
Tb	35	100	500	20	210
Yb	40	200	100	25	190
Lu	30	200	100	25	115
Sc	20	60	60	0	40
Ti	1.2	50	50	0.1	--
Y	35	60	100	40	--
Zr	1.2	1000	2	0.1	--
Nb	0.5	50	2	0.1	--
Hf	0.5	500	10	0.1	65
Ta	0.5	50	2	0	800